





46 hydrothermal fluids reach 155 °C within the upper 21cm below the seafloor (cmbsf) close  
47 to the vent center to near ambient conditions at the vent periphery. The recovered *i*GDGTs  
48 closest to the vent center experienced high rates of turnover with up to 94% of lipid pool  
49 being lost within the upper 21 cmbsf. Here, we show that turnover is non-selective across  
50 TEX<sub>86</sub> GDGT lipid classes and does not independently affect the ratio. However, as evident  
51 by TEX<sub>86</sub> ratios being highly correlated to the Cathedral Hill vent sediment porewater  
52 temperatures ( $R^2 = 0.84$ ), the ratio can be strongly impacted by the combination of severe  
53 lipid loss when it is coupled to the addition of *in situ* *i*GDGT production from archaeal  
54 communities living in the vent sediments. The resulting signal overprint produces absolute  
55 temperature offsets of up to 4 °C based on the TEX<sub>86</sub><sup>H</sup>-calibration relative to modern climate  
56 records of the region. The overprint is also striking given the flux of GDGTs from the upper  
57 water column that is estimated to represent ~93% of the combined intact polar lipid (IPL)  
58 and core GDGT lipid pool initially deposited on the seafloor. A model to correct the  
59 overprint signal using IPLs is therefore presented that can similarly be applied to all near-  
60 surface marine sediment systems where calibration models or climate reconstructions are  
61 made based on the TEX<sub>86</sub> measure.  
62

## 63 1. Introduction

64 Archaeal and bacterial tetraether cellular membrane lipids mark common and structurally  
65 diverse compounds that are frequently used to track the presence of living and dead  
66 microorganisms in the geosphere (e.g. Schouten et al., 2002, 2004; Hopmans et al., 2004;  
67 Weijers et al., 2007; Lipp et al., 2008). The proportional abundances of these lipids forms  
68 various prominent proxies for assessing environmental change through time. For example,  
69 TEX<sub>86</sub> (TetraEther indeX with 86 carbon atoms (Schouten et al. (2002) is the most widely  
70 used archaeal lipid-based paleotemperature proxy for marine environments (Table 1; Eq.  
71 1). This proxy measures variations in the number of cyclopentyl rings within the  
72 hydrocarbon skeleton of a select range of archaeal core lipid (CL) classes (Supplementary  
73 Figure A-1) following the initial assumption that cyclization of the biphytanyl moiety is an  
74 organismal response to changing sea surface temperatures (SSTs). The proxy is therefore  
75 used in paleo-oceanographic studies in many different regions around the world (Huguet et  
76 al., 2006; Kim et al., 2008; McClymont et al., 2012) with TEX<sub>86</sub> values typically ranging  
77 from 0.2–0.9 in both marine and lake sediment (Sinninghe Damsté et al., 2009; Powers et  
78 al., 2010; Zhang et al., 2016 Morrissey et al., 2018; Yao et al., 2019; Kumar et al., 2019).  
79 The utility of TEX<sub>86</sub> rests on the premise that *i*GDGTs found in ocean bottom sediments  
80 are almost exclusively produced by marine planktonic Thaumarchaeota that inhabit the  
81 epipelagic zone (Wakeham et al., 2003; Tierney, 2014). TEX<sub>86</sub>-based lipids are therefore  
82 required to be efficiently and continually transported from the upper water column to the  
83 underlying ocean floor sediments to produce a chemostratigraphic record of microbial  
84 response to changing SST conditions (Wuchter et al., 2005).  
85

86 Since its introduction, the reliability of TEX<sub>86</sub> to accurately track paleoclimate variations  
87 has been questioned. For example, over the past decade, considerable effort has been made  
88 to reconstruct the early Paleogene greenhouse climate with a variety of paleoclimate  
89 proxies (Hollis et al., 2012). However, TEX<sub>86</sub> appears to significantly over-estimate  
90 reconstructed SSTs relative to other proxies such as Mg/Ca, clumped isotopic compositions



91 of foraminiferal calcite, as well as various climate models based on partial pressure of  
92 carbon dioxide ( $p\text{CO}_2$ ) predictions (Lunt et al., 2012; Naafs et al., 2018). The apparent high  
93 SST reconstructions have been attributed to proxy complications including ocean  
94 subsurface sediments origin of lipids (Ho and Laepple, 2016). For late Neogene climate  
95 reconstructions, the proxy has been shown to underestimate warming trends relative to  $U_{37}^{kr}$ -  
96 derived temperatures (Lawrence et al., 2020). In this regard, the debate largely centers on  
97 a lack of understanding of how the proxy's associated lipids precisely change in relation to  
98 their environment and if these changes are regulated by internal adaptations within the  
99 archaeon or by community succession (Elling et al., 2015; Qin et al., 2015).

100

101 Additionally, most Thaumarchaeota are found below the photic and epipelagic zone and  
102 should therefore not produce a direct response to changing SSTs. Studies from the Pacific  
103 Ocean have shown that peak archaeal abundances occur at 100–350 m depth (Karner et al.,  
104 2001; Pearson et al 2013). To address the impact of depth habitat, Schouten *et al.* (2013)  
105 further proposed a calibration based on suspended particulate matter and *in situ* water  
106 temperature from the upper 100 m of the global ocean. In this regard, if these deeper  
107 sourced lipids are deposited on the seafloor than the sedimentary GDGT used to generate  
108 sea surface temperatures are mixed with significant contributions from much colder waters  
109 potentially impacting the reconstructed values providing much lower SSTs. As  $\text{TEX}_{86}$  may  
110 become disproportionality impacted by the collection of mixed source inputs; the location  
111 of lipid loading from the water column to the ocean floor sediments seems to be an factor  
112 as strong positive relationship between water depth and differences in  $\text{TEX}_{86}^H$  values are  
113 observed in both surface sediments and suspended particulate organic matter from the  
114 Mediterranean Sea (Kim et al., 2015). The differences appear to be driven by increase  
115 relative abundances of  $\text{TEX}_{86}$  lipids GDGT-2 and the isomers of crenarchaeol (Lui et al.,  
116 2018; Damsté et al., 2018) coupled to decreasing abundances of GDGT-1 and GDGT-3  
117 with increasing water depth. The systematic change results in a higher reconstructed SST  
118 bias for deep-water surface sediments. Therefore, such sourcing effects have further  
119 resulted in speculation that the  $\text{TEX}_{86}$  ratio of open ocean sediments may actually reflect  
120 deeper water column and subsurface rather than SSTs (Huguet et al., 2007; Lopes dos  
121 Santos *et al.*, 2010; Kim *et al.*, 2012a,b; Ho & Laepple, 2016; Hurley et al., 2016). To  
122 compensate for this, both  $\text{TEX}_{86}^H$  and  $\text{TEX}_{86}^L$  have been re-calibrated against subsurface (0–  
123 900 m water depth) temperatures (Kim *et al.*, 2012a,b; Ho & Laepple, 2016).

124

125 The GDGT relative abundances recorded in a  $\text{TEX}_{86}$  measurements may constitute a multi-  
126 variable system, having both a component of lipids contributed to the “pool” via *in situ*  
127 sources and by depositional processes.  $\text{TEX}_{86}$ -based SST estimates have been observed to  
128 substantially deviate from other temperature proxies (e.g., Huguet et al., 2006; Liu et al.,  
129 2009; Rommerskirchen et al., 2011; Hollis et al., 2012; Seki et al., 2012) implying these  
130 values can be a response to seasonal biases, non-thermal influences, or other ecological  
131 signals. Non-thermal influence result from lipid abundances being brought to marine  
132 sediments from non-planktonic Thaumarchaeota origins such as from the deep water or  
133 within marine sediments (Liu et al., 2011; Kerou et al. 2020). There are likely other driving  
134 forces other than temperature that impact the archaeal GDGT production and relative  
135 abundances. Some examples of these drivers include organismal selectivity to specific



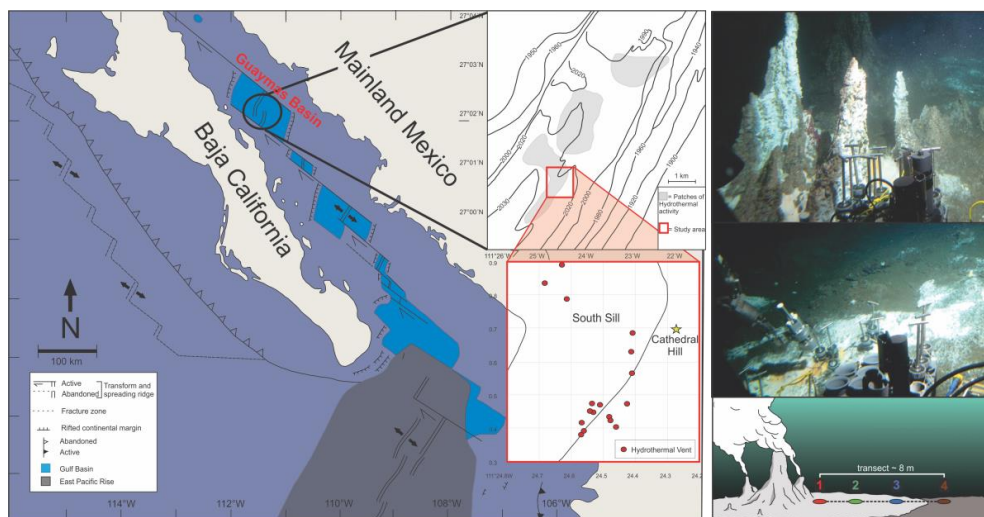
136 growth phases and growth rates (Elling et al., 2014; Hurley et al., 2016); ammonia  
137 oxidation rates (Hurley et al., 2016); and redox conditions (Qin et al., 2015).

138

139 By artificially hydrolyzing the headgroups of marine archaeal IPLs harvested from a  
140 sediment trap, Lipp and Hinrichs (2009) demonstrated that the production of GDGTs by  
141 ocean floor sediment microbial communities may impact TEX<sub>86</sub> values. Similarly, Elling  
142 et al. (2015) confirmed TEX<sub>86</sub> values can represent a mixed GDGT signal from both active  
143 microbial production in shallow sediments and fossil lipids sourced from the water column.  
144 These authors further demonstrated that TEX<sub>86</sub> values from cultures can diverge from the  
145 global calibration that forms the basis for most climate reconstructions suggesting that the  
146 sedimentary community compositions may exert some controls on the TEX<sub>86</sub> signal.  
147 Besseling et al. (2019) further extended these concerns, suggesting TEX<sub>86</sub> reflects  
148 subsurface temperatures rather than SSTs as the input of GDGTs in marine settings are not  
149 exclusive to Thaumarchaeota, because a majority of marine group I (MGI) Archaea also  
150 reside in subsurface waters or marine sediments. Collectively, these observations indicate  
151 a sub-pelagic zone where microorganisms may mix with the GDGTs from the surface, thus  
152 providing mixed signals and inaccurate TEX<sub>86</sub> values from mixed sources. However, other  
153 authors have found that TEX<sub>86</sub> ratios are not impacted by benthic Archaea due to the low  
154 relative turnover rates for the lipids in marine sediments (Lengger et al., 2012, 2014; Omuh  
155 et al., 2020). Omuh et al. (2020) found little effect to the TEX<sub>86</sub> paleoclimate ratio when  
156 examining surface sediments near hydrothermal vent sites on the Southeast Indian Ridge  
157 in the southern Indian Ocean. Lengger et al. (2012, 2014) reported no significant deviation  
158 between the TEX<sub>86</sub> values in sediment cores collected near the oxygen minimum zone from  
159 that of the overlying water column in the Arabian Sea with near linear degradation rates of  
160 both IPLs and CLs.

161

162 While not an ideal location to create SST reconstructions, hydrothermal vents of  
163 sedimented ocean basins do represent an anomalous end-member to the vast expanse of  
164 ambient ocean floor sediment where paleoclimate reconstructions are commonly produced.  
165 The Guaymas Basin, Gulf of California (Figure 1) is one such site. The basin experiences  
166 elevated sedimentation rates ranging between 0.4–0.2 cm/yr. (Curry et al., 1979; Gieskes  
167 et al., 1988) due in part to the high productivity of the upper water column. The ocean floor  
168 hydrothermally impacted surface sediments are also a location of active and diverse  
169 microbial communities with vents that are often covered by Beggiatoa dominated microbial  
170 mats (Teske et al., 2016). These sites should in principle enable a high-resolution archaeal  
171 lipid-based paleoclimate record that provides optimal conditions for studying potential  
172 subsurface lipid overprinting or interferences to common archaeal lipid-based  
173 environmental proxies. For this study, we examined near-surface ocean floor sediments  
174 from the Cathedral Hill hydrothermal vent complex (Figure 1) in the Guaymas Basin to  
175 determine if sea surface paleoclimate proxy signals can be impacted by the presence of  
176 subsurface archaeal populations. The distribution of GDGTs and their corresponding  
177 environmental proxy signals were measured within the sediments along a transect at the  
178 Cathedral Hill hydrothermal vent system. In this regard, this site offers the unique  
179 opportunity to evaluate the response of TEX<sub>86</sub> and other tetraether-lipid proxies within a  
180 microbially diverse sedimentary environment that is exposed to high temperature vent  
181 fluids.



182

183 **FIGURE 1** A) Location map of Guaymas Basin and the Southern Sill (red outlined box)  
184 in the Gulf of California. Cathedral Hill is marked with a yellow star. B) Photo of Cathedral  
185 Hill taken via *Alvin*. C) Schematic of the push core transect with a color coding that is  
186 consistent for all plots throughout this paper. Maps modified from Teske et al. (2016) and  
187 Dazell et al. (2021).

188

## 189 2. Material and methods

### 190 2.1. Study location and sampling

191 Four sediment push cores were collected using HOV *Alvin* (Dive 4462; 10/22/08) at the  
192 Cathedral Hill hydrothermal vent site, located at a water depth of 1996 m in the Southern  
193 Trough of Guaymas Basin, Gulf of California (27°0.629' N, 111°24.265' W) (Figure 1).  
194 The push cores, labeled 1 to 4, were taken along a transect with ~ 2 m spacing extending  
195 outwards from microbial mat-covered sediments near the sulfide chimney complex to just  
196 outside of the microbial mat area in ambient seafloor sediment. Thermal-probe  
197 measurements were taken next to each core (Table 1). Once the push cores were brought  
198 to the surface, they were subsampled into 2–3 cm-thick intervals, transferred to combusted  
199 glass vials and immediately stored at -40 °C (onboard the ship) before being shipped under  
200 dry ice to the laboratory and later freeze-dried and stored at -80 °C until being later  
201 processed.

202

203

204

205

206

207

208

209



210 **Table 1.** Sediment geochemical and lipid proxy data.

211

Core <sup>na</sup>	Depth interval (cmbfs)	Alvin dive # and core ID	Description/lithology <sup>nb</sup>	Pore water temperature (°C)	Interpolated Pore water temperature (°C)	Sediment weight (g)	TLE µg/g sediment
1	0-2	GB4462-5	Black mud with microbial mat filaments	19	19	2.40	11552.3
1	2-4	GB4462-5	Brownish-green diatomaceous mud	-	67	2.10	7648.2
1	4-6	GB4462-5	Brownish-green diatomaceous mud	85	85	2.04	9266.0
1	6-8	GB4462-5	Brownish-green diatomaceous mud	-	105	2.83	2088.3
1	8-10	GB4462-5	Brownish-green diatomaceous mud	-	117	2.48	4378.1
1	10-12	GB4462-5	Grayish-green mud	121, 124	125	2.52	1972.2
1	12-15	GB4462-5	Brownish-green consolidated mud with clay shards	-	135	2.62	1992.4
1	15-18	GB4462-5	Brownish-green consolidated clay	142	145	3.01	1691.0
1	18-21	GB4462-5	Brownish-green consolidated clay	153	153	2.94	1722.0
2	0-2	GB4462-6	Black mud with microbial mat filaments	9, 13	11	2.12	8476.2
2	2-4	GB4462-6	Black mud with microbial mat filaments	-	22	2.30	8653.5
2	4-6	GB4462-6	Brownish-green diatomaceous mud	20	20	3.30	2509.2
2	6-8	GB4462-6	Brownish-green diatomaceous mud	-	47	2.84	3383.8
2	8-10	GB4462-6	Brownish-green diatomaceous mud	-	60	3.34	1480.5
2	10-12	GB4462-6	Brownish-green diatomaceous mud	69, 77	73	2.39	4185.9
2	12-15	GB4462-6	Brownish-green diatomaceous mud	-	87	3.50	1694.3
2	15-18	GB4462-6	Brownish-green diatomaceous mud	118	105	3.50	2011.6
2	18-21	GB4462-6	Brownish-green diatomaceous mud	109	125	3.48	1382.2
3	0-2	GB4462-3	Black mud with microbial mat filaments	3.2	3.2	2.81	7313.2
3	2-4	GB4462-3	Brownish-green diatomaceous mud	-	8	2.88	3909.7
3	4-6	GB4462-3	Brownish-green diatomaceous mud	15	15	2.45	2864.8
3	6-8	GB4462-3	Brownish-green diatomaceous mud	-	26	2.80	5003.6
3	8-10	GB4462-3	Brownish-green diatomaceous mud	34	34	2.80	2018.0
3	10-12	GB4462-3	Brownish-green diatomaceous mud	-	43	3.15	1863.5
3	12-15	GB4462-3	Brownish-green diatomaceous mud	-	54	3.15	1777.8
3	15-18	GB4462-3	Brownish-green diatomaceous mud	61	66	2.45	1428.6
3	18-21	GB4462-3	Brownish-green diatomaceous mud	83	80	2.80	1982.0
4	0-2	GB4462-8	Black mud	0	0	2.80	3440.4
4	2-4	GB4462-8	Brownish-green diatomaceous mud	1.5	8	2.80	3166.1
4	4-6	GB4462-8	Brownish-green diatomaceous mud	16	16	2.55	4000.0
4	6-8	GB4462-8	Brownish-green diatomaceous mud	-	18	2.80	4185.5
4	8-10	GB4462-8	Brownish-green diatomaceous mud	-	21	3.33	4755.3
4	10-12	GB4462-8	Brownish-green diatomaceous mud	-	23	2.44	4843.6
4	12-15	GB4462-8	Brownish-green diatomaceous mud	-	25	0.32	5741.9
4	15-18	GB4462-8	Sample lost during collection	-	-	-	-
4	18-21	GB4462-8	Sample lost during collection	29	-	-	-

212

213

214

215

216

217

218

219

220

221

222 **Table 1.** Sediment geochemical and lipid proxy data (continued).

223



Core <sup>a</sup>	Depth interval (cmbsf)	Alvin dive # and core ID	TEX <sub>86</sub> Core GDGT <sup>c</sup>	TEX <sub>86</sub> <sup>H</sup> Core GDGT <sup>d</sup>	TEX <sub>86</sub> <sup>H</sup> Reconstructed SSTs (Kim et al., 2010) <sup>e</sup>	RI <sup>f</sup>	MI <sup>g</sup>	TEX <sub>86</sub> 1G-GDGT <sup>c</sup>	TEX <sub>86</sub> Core GDGT <sup>c</sup>
1	0-2	GB4462-5	0.56	-0.25	21.2	2.44	0.34	0.58	0.56
1	2-4	GB4462-5	0.58	-0.23	22.6	2.45	0.38	0.58	0.58
1	4-6	GB4462-5	0.58	-0.24	22.3	2.48	0.36	0.55	0.58
1	6-8	GB4462-5	0.58	-0.24	22.2	2.55	0.35	0.57	0.58
1	8-10	GB4462-5	0.59	-0.23	22.9	2.60	0.34	0.72	0.59
1	10-12	GB4462-5	0.57	-0.25	21.8	2.63	0.31	0.70	0.57
1	12-15	GB4462-5	0.61	-0.22	23.8	2.65	0.37	0.69	0.61
1	15-18	GB4462-5	0.61	-0.22	23.9	2.66	0.36	-	0.61
1	18-21	GB4462-5	0.63	-0.20	24.9	2.66	0.38	-	0.63
2	0-2	GB4462-6	0.55	-0.26	20.6	2.524	0.32	0.46	0.55
2	2-4	GB4462-6	0.54	-0.27	20.4	2.524	0.32	0.58	0.54
2	4-6	GB4462-6	0.54	-0.27	20.4	2.525	0.33	0.60	0.54
2	6-8	GB4462-6	0.56	-0.25	21.5	2.677	0.29	0.71	0.56
2	8-10	GB4462-6	0.58	-0.25	21.7	2.695	0.29	0.70	0.58
2	10-12	GB4462-6	0.57	-0.24	21.9	2.712	0.28	0.68	0.57
2	12-15	GB4462-6	0.57	-0.24	21.9	2.734	0.28	0.73	0.57
2	15-18	GB4462-6	0.58	-0.23	22.6	2.680	0.31	-	0.58
2	18-21	GB4462-6	0.59	-0.23	22.8	2.738	0.28	-	0.59
3	0-2	GB4462-3	0.54	-0.27	20.2	2.41	0.37	0.53	0.54
3	2-4	GB4462-3	0.53	-0.27	19.8	2.62	0.27	0.49	0.53
3	4-6	GB4462-3	0.53	-0.27	19.9	2.53	0.31	0.56	0.53
3	6-8	GB4462-3	0.54	-0.27	20.3	2.50	0.33	0.54	0.54
3	8-10	GB4462-3	0.53	-0.27	19.9	2.54	0.31	0.61	0.53
3	10-12	GB4462-3	0.54	-0.27	20.3	2.64	0.27	0.74	0.54
3	12-15	GB4462-3	0.56	-0.25	21.5	2.56	0.30	0.69	0.56
3	15-18	GB4462-3	0.55	-0.26	20.9	2.77	0.26	0.74	0.55
3	18-21	GB4462-3	0.57	-0.25	21.6	2.68	0.29	0.66	0.57
4	0-2	GB4462-8	0.54	-0.27	20.4	2.43	0.35	0.54	0.54
4	2-4	GB4462-8	0.53	-0.27	20.0	2.59	0.30	0.37	0.53
4	4-6	GB4462-8	0.54	-0.27	20.2	2.55	0.31	0.43	0.54
4	6-8	GB4462-8	0.52	-0.28	19.3	2.55	0.29	0.45	0.52
4	8-10	GB4462-8	0.53	-0.27	19.9	2.69	0.26	-	0.53
4	10-12	GB4462-8	0.53	-0.27	19.8	2.54	0.30	-	0.53
4	12-15	GB4462-8	0.53	-0.28	19.7	2.90	0.20	-	0.53
4	15-18	GB4462-8	-	-	-	-	-	-	-
4	18-21	GB4462-8	-	-	-	-	-	-	-

224 <sup>a</sup> Collected core numbers are relabelled in the sample name to reflect a relative transect position (1-4).

225 <sup>b</sup> Sediment lithology based on freeze-dried sediments.

226 <sup>c</sup>  $TEX_{86} = (GDGT-2 + GDGT-3 + GDGT-5') / (GDGT-1 + GDGT-2 + GDGT-3 + GDGT-5')$ , (Schouten et al., 2002)

227 applied to both core GDGTs and 1-glycosyl-GDGTs. (1)

228 <sup>d</sup>  $TEX_{86}^H = \log ((GDGT-2 + GDGT-3 + GDGT-5') / (GDGT-1 + GDGT-2 + GDGT-3 + GDGT-5'))$ , for sediments

229 outside the polar regions (Kim et al., 2010).

230 <sup>e</sup> Following the mean annual sea surface calibration of 0 m water depth ( $SST = 68.4 \times TEX_{86}^H + 38.6$ ) of Kim et al.

231 (2010).

232 <sup>f</sup> Ring index (RI) =  $0 \times (GDGT-0) + 1 \times (GDGT-1) + 2 \times (GDGT-2) + 3 \times (GDGT-3) + 4 \times (GDGT-4) + 5 \times (GDGT-5) /$

233  $\Sigma GDGTs$ , adapted from Pearson et al. (2004). (2)

234 <sup>g</sup> Methane index (MI) =  $(GDGT-1 + GDGT-2 + GDGT-3) / (GDGT-1 + GDGT-2 + GDGT-3 + GDGT-5 + GDGT-5')$  by

235 Zhang et al. (2011).

236

237

238 **2.2. Lipid extraction**



239 Samples were spiked with a recovery standard (1-alkyl-2-acetoxy-*sn*-glycero-3-  
240 phosphocholine (PAF); Avanti Polar Lipids, Inc.) and extracted using a modified Bligh and  
241 Dyer protocol after Sturt et al. (2004). The extraction involved six steps using 3 different  
242 solvent mixtures. The first four steps involved solvent mixtures of  
243 methanol/dichloromethane/buffer [2:1:0.8; v/v]. From this, the first two steps used a  
244 phosphate buffer (5.5 g/L Na<sub>2</sub>HPO<sub>4</sub>; Avantor Performance Materials, LLC.) adjusted to pH  
245 of 7.4 with HCl; Anachemia Co.), while the third and fourth steps employed a  
246 trichloroacetic acid buffer (50 g/L C<sub>2</sub>HCl<sub>3</sub>O<sub>2</sub>; Avantor Performance Materials, LLC. (pH of  
247 2). The final two steps used a solvent mixture of methanol/dichloromethane [5:1; v/v]. Each  
248 extraction step consisted of a 6 ml of solvent mixture, sonicated for 5 min. and centrifuged  
249 for 5 min. at 1250 rpm. After each extraction step, the solvent was decanted and combined  
250 in a separation funnel. The combined extract was purified with milliQ water, heated at ca.  
251 60 °C, and evaporated to dryness under a gentle steam of dry nitrogen. The resulting total  
252 lipid extract (TLE) was then spiked with 1, 2-diheneicosanoyl-*sn*-glycero-3-  
253 phosphocholine (C<sub>21</sub>-PC; Avanti Polar Lipids, Inc.) and subsequently stored at -20 °C  
254 before it was injected for mass spectral analysis.  
255  
256

### 257 2.3. High performance liquid chromatography – mass spectrometry (HPLC-MS)

258

259 A reverse phase electrospray ionization method with a scan range from 100–3000 *m/z* was  
260 chosen for its ability to simultaneously resolve archaeal IPLs and CLs. An aliquot of each  
261 sample representing 1% of the TLE was analyzed using an Agilent Technologies 1260  
262 Infinity II HPLC coupled to an Agilent Technologies 6530 quadrupole time-of-flight mass  
263 spectrometer (qToF-MS). Separation was achieved following the method described by Zhu  
264 et al. (2013) using an Agilent Technologies ZORBAX RRHD Eclipse Plus C<sub>18</sub> (2.1 mm ×  
265 150 mm × 1.8 μm) reverse phase column, fitted with a guard column and maintained at 45  
266 °C. The flow rate was set to 0.25 mL/min. and the gradients were: mobile phase A  
267 (methanol/formic acid/ammonium hydroxide [100:0.04:0.10] v:v:v) held at 100% for 10  
268 min., followed by a linear gradient to 24% mixing with mobile phase B (propan-2-ol/formic  
269 acid/ammonium hydroxide [100:0.04:0.10] v:v:v) extending for 5 min., a linear gradient to  
270 65% B for 75 min., followed by 70% B for 15 min., that finished by re-equilibrating with  
271 100% A for 15 min. The injection solvent was methanol.  
272

273 Analyte identification was achieved by accurate mass resolution, mass spectral analysis  
274 using Agilent Technology's MassHunter software and by comparison of fragmentation  
275 patterns with the literature (e.g., Knappy et al., 2009; Liu et al., 2010; Yoshinaga et al.,  
276 2011). Quantification was achieved by summing the integration of peak areas of adducts  
277 [M+H]<sup>+</sup>, [M+NH<sub>4</sub>]<sup>+</sup>, and [M+Na]<sup>+</sup> for the respective GDGTs of interest. The signals for  
278 these compounds were monitored as [M+H]<sup>+</sup> on the *m/z* 1464.38, 1462.36, 1460.34,  
279 1458.33 1456.31, 1454.30 mass chromatograms. Additionally, mass fragments consistent  
280 with the loss of a biphytane (*m/z* 743.7) were observed. Once the integrated peak areas were  
281 determined for each GDGT, concentration values were obtained relative to the internal C<sub>21</sub>-  
282 PC standard and reported in μg/g dry sediment weight.  
283

284 Response factors were determined by a series of injections of a standard solution  
285 containing; 1,2-diacyl-3-O-(α-D-galactosyl-1-6)-β-D-galactosyl-*sn*-glycerol (DGDG), 1,2-



286 diacyl-3-O- $\beta$ -D-galactosyl-*sn*-glycerol (MGDG), 1-alkyl-2-acetoxy-*sn*-glycero-3-  
287 phosphocholine (PAF), 1,2-di-O-phytanyl-*sn*-glycerol (Archaeol), 1',3'-bis[1,2-  
288 dimyristoyl-*sn*-glycero-3-phospho]-glycerol (14:0 Cardiolipin), 1,2-diheneicosanoyl-*sn*-  
289 glycero-3-phosphocholine (C<sub>21</sub>-PC) from Avanti Polar Lipids, Inc., USA, and 2,2'-di-O-  
290 decyl-3,3'-di-O-(1'', $\omega$ ''-eicosanyl)-1,1'-di-(rac-glycerol) (C<sub>46</sub>-GTGT) from Pandion  
291 Laboratories, LLC in amounts ranging from 100 pg to 30 ng. Concentrations of the standard  
292 mix were then calculated from peak areas of molecular ions in mass chromatograms.  
293 Response factors were calculated relative to the C<sub>21</sub>-PC, and the appropriate correction  
294 factor was applied to the particular lipid class of interest.

295  
296 A series of samples were re-run to identify or confirm deviations in the data set. The  
297 variations between the concentrations of GDGTs in the re-run and the initial runs yielded a  
298 maximum difference of  $\sim \pm 4 \mu\text{g/g}$  per GDGT compound, providing confidence in the initial  
299 results and confirming the presence of two outliers in the data set. These outliers are Core 4  
300 at 8-10 cm, with abnormally low concentrations of all compounds that is likely ion  
301 suppression from a sample heavily impregnated with oil, and Core 3 at 15–18 cm, which  
302 contains relatively high lipid concentrations that are yet to be explained.

303

304

### 305 3. Results and Discussion

#### 306 3.1. Archaeal lipid diversity and heterotrophic loss

307 The Cathedral Hill transect sediments have *i*GDGTs containing 0–4 cyclopentyl (GDGT  
308 0–4) as well as crenarchaeol (Cren) and the isomer of crenarchaeol (Cren') that contains  
309 five rings (four cyclopentyl and one cyclohexyl moiety) (Table S1). Branched GDGTs  
310 include 1a-c, 2a-c, and 3a were found to have discontinuous and/or low absolute  
311 abundances, with some compound classes not being detected (i.e. *br*GDGT-3b). The  
312 *br*GDGTs are therefore not further examined in this study. For cores 1 to 3 the  
313 concentrations of all *i*GDGT compounds systematically decrease with depth (Figure 2).  
314 Bentley et al. (2021) established the sedimentation of archaeal lipids from the upper water  
315 column as being uniform both in terms of spatial loading across the length of the transect  
316 as well as over the past 52.5–105 yrs. of sedimentation penetrated by the length of the push  
317 core. From this, it is estimated that  $\sim 70.57 \pm 23.5 \mu\text{g } i\text{GDGTs/g sed./yr.}$  is being deposited  
318 on the seafloor from the upper water column. However, for cores closest to the vent site,  
319 lipid abundances exhibited a much sharper decrease with depth, which Bentley et al. (2021)  
320 attribute to the turnover of archaeal lipids coupled to, but not directly caused by,  
321 hydrothermalism. For cores 1 and 2, losses reach as high as 94% within the upper 21 cmbsf  
322 (cm below sea floor). The lipid loss is less severe for core 3 at  $\sim 60\%$ . For the ambient core  
323 4, *i*GDGTs have similar down core stratigraphic trends with a near-consistent average of  
324  $400 \mu\text{g/g}$  sediment concentration and no systematic loss of lipids.

325

326 Due to the extreme vent conditions at Cathedral Hill, the identified archaeal *i*GDGT-based  
327 IPLs within the sediments most likely represent the composition of cellular membrane  
328 material from active archaeal communities residing in the sediments. These lipids have  
329 exclusively monoglycosyl (1G) or diglycosyl (2G) head groups linked to a 2,3-*sn*-glycerol.  
330 Within the pyrolytic environment the transformation of IPL *i*GDGTs could hypothetically



331 add to the core *i*GDGT lipid pool. Similar to CLs, the 1G-GDGTs range from -0 to -4 and  
 332 include Cren and Cren'. Surface concentrations of these lipids are ~15 µg/g sed. in cores 1  
 333 to 3 (residing within the microbial mat) and 11 µg/g sed. for core 4 (Table S2). Also similar  
 334 to the CLs, the archaeal IPL concentrations decrease down core and are tightly controlled  
 335 by porewater temperatures (Table S2). For cores 1 and 2 the maximum depths for  
 336 detectable 1G-GDGTs are 15–18 and 12–15 cmbsf, corresponding to vent porewater  
 337 temperatures of 145 and 87 °C, respectively. In core 3, 1G-GDGTs persists down core with  
 338 a consistent lipid depletion that reaches its lowest concentration of 5.22 µg/g sed. in the  
 339 bottom of the core at 18–21 cmbsf sediment depth where porewater temperatures rise to 80  
 340 °C. In core 4, which is most similar to the ambient ocean bottom conditions and falls outside  
 341 of the area covered by the microbial mat, the lipid concentrations average is ~8 µg/g sed.  
 342 across the depth of the core. The 2G-GDGTs have 0 to 2 cyclopentyl rings that for cores 1  
 343 and 2 are restricted to the upper 4 to 6 cmbsf. These lipids are not further investigated in  
 344 this study as 2G-GDGTs are of limited abundance (max summed concentrations <7 µg/g  
 345 sed.) and their structural diversities negligibly effect isoprenoid-based proxies.

346  
 347 Lipid-based proxies for the calibration or reconstruction of paleoclimate records such as  
 348 TEX<sub>86</sub>, BIT, CBT, and MBT, are based on environmentally scaled loadings of select GDGT  
 349 compound classes. These proxies could be negatively impacted should other ocean floor  
 350 sediment systems experience high rates of lipid turnover (Lengger et al., 2014). To evaluate  
 351 whether down-core depletions of lipid concentrations impacted tetraether-based proxies,  
 352 the concentrations of the highly abundant GDGT-0 was plotted relative to the TEX<sub>86</sub> ratio  
 353 lipids (*i*GDGT-1, -2, -3, and Cren') (Figure 3A). For figure 3A, straight lines in the  
 354 logarithmic plot indicate near-equal depletion rates between the paired x- and y-axis lipid  
 355 classes. Similarly, parallel lines between lipid pairs also indicates near-equal depletion  
 356 rates, with vertical offsets between pairs marking different initial starting abundances  
 357 between the paired lipid classes. In this regard, *i*GDGT-0, -1, -2, and Cren' have undergone  
 358 the same rate of turnover. However, the depletion rate of *i*GDGT-3's is lower than that of  
 359 other lipid classes for cores 1 and 2. Although, this may represent a distinct resilience to  
 360 turnover, we suggest it results from overprinting by the subsurface hyperthermophilic  
 361 archaeal community (see below).

362 To better track changes across each core, the degradation rate constants (*k'*) of TEX<sub>86</sub> lipid  
 363 classes were calculated for each push core (Figure A2; Table A3) using a first-order kinetic  
 364 model:

$$C_t = C_i e^{-k't} \quad (5)$$

368 in which *C<sub>t</sub>* and *C<sub>i</sub>* are concentration at time (*t*) and the initial concentration, respectively  
 369 (Schouten et al., 2010). Rearranging Eq. 5, the *k'* were calculated as

$$k' = (-\ln[C_t / C_i]) / t \quad (6)$$

373 From these data, it is evident that the down core concentrations of each lipid decrease at  
 374 equivalent rates for all but core 2 (i.e. they have the same slopes for their rates of decay;

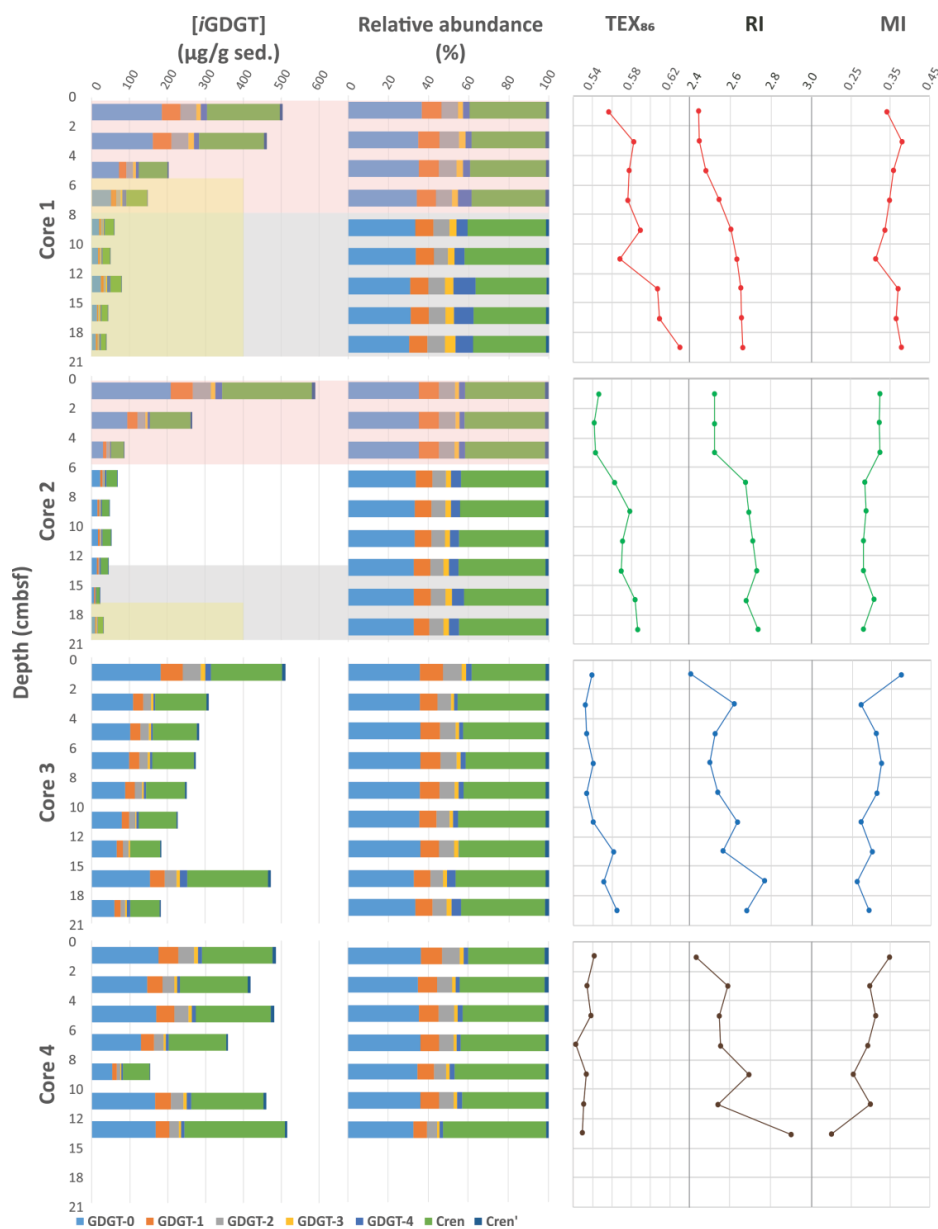


375  $m_{\log k}$ ). This is consistent with the  $TEX_{86}$  *i*GDGT lipid classes being removed from the  
376 sediment lipid pool in a non-selective manner.

377 Lastly,  $TEX_{86}$ , RI, and MI values were plotted against their respective summed *i*GDGTs  
378 lipid concentrations (Fig 3B–D). For samples located within the habitable zone (having  
379 porewaters ranging from 0–123 °C; Kashefi and Lovley, 2003), no correlation is observed  
380 between the lipid abundances and proxy ratios of  $TEX_{86}$ , RI, or MI (Figure 3B–D). This  
381 further suggests these proxies are not affected by turnover in the habitable zone. However,  
382 once sediment burial reaches beyond the habitable zone,  $TEX_{86}$  ratios trend to higher values  
383 (similarly also reflected in GDGT-3 concentration trends of Figure 3A). Collectively, these  
384 data strongly indicate that archaeal lipid turnover is largely nonselective of the  $TEX_{86}$  lipid  
385 classes and will therefore theoretically not in and of itself significantly impact archaeal  
386 lipid paleoclimate proxy reconstructions.

387  
388 Apart from paleoclimate reconstructions, the archaeal lipid data can also be used to resolve  
389 some aspects of the local biogeochemical cycles present at the vent site. Maximal anaerobic  
390 oxidation of methane (AOM) at Guaymas Basin has been observed at 35 to 90 °C, but  
391 generally accounts for less than 5% of sulfate reduction (Kallmeyer and Boetius, 2004).  
392 For example, highly  $^{13}C$ -depleted CLs reaching up -70‰ in hydrothermal vent sediments  
393 with porewater temperatures as high as 95 °C indicates thermophilic archaea actively  
394 engaging in AOM (Schouten et al., 2003). The methane index (MI; Table 1) can be used to  
395 differentiate regions of normal marine (values between 0–0.3) and active AOM conditions  
396 where values >0.5–1 for gas hydrate impacted sediments and subsurface environments with  
397 high levels of AOM (Stadnitskaia et al., 2008, Zhang et al., 2011). When applying the MI  
398 to the Cathedral Hill sediments very low values are recorded with no correspondence to  
399 thermal controls. Although, it could be considered that this arises from selective  
400 degradation; the very low MI values are equally explained by broad loading of *i*GDGTs  
401 from the upper water column. As such, the low AOM activities may also indicate microbial  
402 ammonia oxidation, which has been shown to influence the  $TEX_{86}$  proxy (Hurley et al.,  
403 20016) is likely not a significant factor in this setting.

404

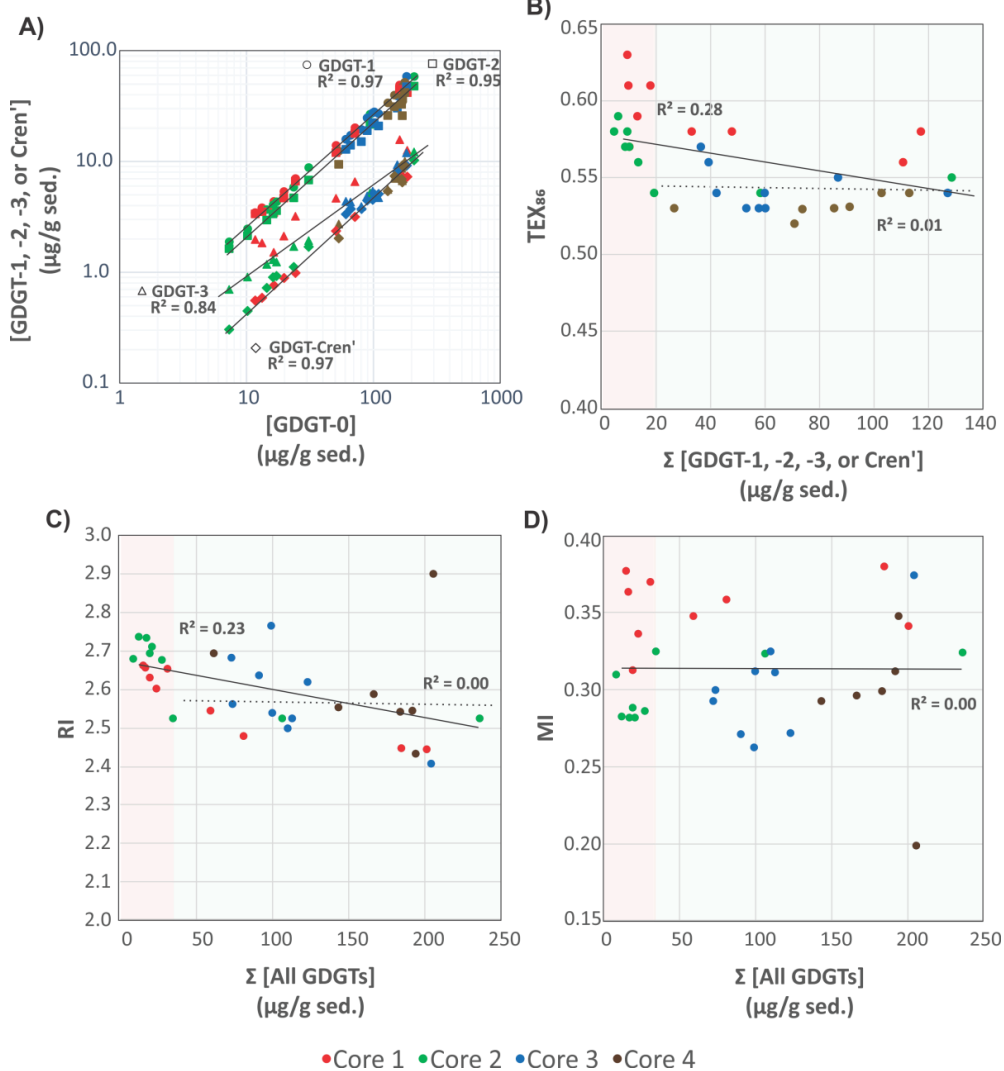


405  
 406  
 407  
 408  
 409  
 410  
 411  
 412  
 413

**FIGURE 2.** Down core profiles of the Cathedral Hill core *i*GDGTs absolute and relative lipid abundances and their generated *i*GDGT proxies: TEX<sub>86</sub>, RI, and MI. Pink regions indicate transect intervals within zones of active GDGT lipid heterotrophy (Bentley et al., 2021). Grey regions mark regions where porewater temperatures exceeded 123 °C marking a zone beyond the upper thermal limit of life. Yellow fields indicate regions where oil generation and hydrocarbon degradation has been noted to occur (Dalzell et al., 2021).



414



415  
 416

417 **FIGURE 3.** A) Comparison of  $TEX_{86}$  lipid concentrations GDGT-1 (circles), -2 (squares),  
 418 -3 (triangles), and Cren' (diamonds) relative to the GDGT-0. Comparison of B)  $TEX_{86}$ , C)  
 419 RI, and D) MI proxy values relative to summed  $iGDGTs$  abundances of the Cathedral Hill  
 420 transect cores. Light green and pink regions indicate areas within and outside the habitable  
 421 zone of life. Solid and dotted regression lines mark the total number of samples investigated  
 422 for this study ( $n=34$ ) and those that only reside within the habitable zone where up to 94%  
 423 of the archaeal lipid turnover occurs ( $n=22$ ), respectively.

424  
 425



### 426 3.2. TEX<sub>86</sub> and reconstructed SSTs

427

428 McClymont et al. (2012) reported a GDGT-based reconstructed annual SSTs of 16–18 °C  
429 for ambient sediment in the Guaymas Basin during an annual cycle from 1996–1997  
430 following the calibration model for sediments outside of polar regions proposed by Kim et  
431 al. (2010). These authors demonstrated the temperatures derived from the TEX<sub>86</sub>  
432 reconstruction were significantly lower than those derived from the closely co-varying U<sub>37</sub><sup>kr</sup>,  
433 an alkenone lipid-based paleoclimate proxy (Brassell et al., 1986), and satellite measured  
434 estimates that jointly produced a mean annual sea surface temperature (MASST) of 23 °C.  
435 The longer 21-year (1982–2004) satellite-derived MASST is also reported to be higher at  
436 24 °C (Herrera-Cervantes et al., 2007). Although the sites and time frames of these surveys  
437 do not match that of the Cathedral Hill survey, they do provide context to what our  
438 reconstructed TEX<sub>86</sub> values should record.

439

440 The high sedimentation rate at Cathedral Hill has resulted in near homogenous inputs of  
441 organic matter from the upper water column across the transect area (Dalzell et al., 2021;  
442 Bentley et al., 2021). Therefore, TEX<sub>86</sub> reconstructions should produce equivalent cross-  
443 transect trends with sediment depth. Nonetheless, as with changes in the archaeal lipid  
444 concentrations, the profiles of *i*GDGT proxies TEX<sub>86</sub> and RI of the transect similarly have  
445 down core trends (Figure 2; Bentley et al., 2021). For core 4, TEX<sub>86</sub> span a narrow range  
446 of values (n=7; 0.52–0.54, avg. 0.53 ± 0.01; Figure 4A) across a period of ~ 37.5 to 75 yrs.  
447 To a slightly lesser degree, the shallow-surface samples (0–2 cmbsf) across the transect also  
448 display near-equal values to core 4 (n=4; 0.56–0.54; avg. 0.55 ± 0.01). These values mark  
449 a TEX<sub>86</sub><sup>H</sup> reconstructed mean annual SST of 19.3–20.4 °C following the Kim et al. (2010)  
450 calibration model (Table 1). However, the TEX<sub>86</sub> values recorded in cores 1 to 3 at  
451 Cathedral Hill have considerably larger ranges that systematically increase with rising  
452 porewater temperatures (R<sup>2</sup> = 0.83; Table 1; Figure 2 and 4A). This increase is most  
453 noticeable in core 1 where the highest TEX<sub>86</sub> values are obtained from the bottom core  
454 sediments (10–21 cmbsf) where TEX<sub>86</sub> values span 0.57–0.63 (Table 1; Fig 4A)  
455 corresponding to a TEX<sub>86</sub><sup>H</sup> reconstructed SST change of 3.1 °C marking a range from 21.8  
456 to 24.9 °C (Table 1). Since the Cathedral Hill transect only spans ~8 m, the fundamental  
457 driver for the proxy's increases must be exposure to *in situ* vent fluid temperatures (Figure  
458 4).

459

460 Two mechanisms are considered for the observed proxy variations. The first is that  
461 progressive ring-loss due to carbon-carbon bond cleavage of pentacyclic rings moieties by  
462 exposure to the sharp geothermal gradient at Cathedral Hill acts to systematically attenuate  
463 the *i*GDGT lipid pool. Hydrous pyrolysis experiments conducted by Schouten et al. (2004)  
464 demonstrated that at extreme temperatures (ca. >160 °C), TEX<sub>86</sub> values become negatively  
465 impacted by the preferential destruction of polycyclic GDGTs. Such losses produce  
466 progressively lower ratio values. Although, the transect sediment porewaters do not reach  
467 the pyrolytic temperatures of the Schouten et al. (2004) experiment, they are high enough  
468 to generate hydrocarbons (Dalzell et al., 2021) and thermochemically degrade *i*GDGTs in  
469 the hottest regions of the transect. However, the observed stratigraphic TEX<sub>86</sub> trends do not  
470 match those of predicted ring loss as the values increase rather than decrease in relation to



471 elevated porewater condition. Nonetheless, the thermochemical oxidative loss of GDGTs  
472 and its effect on the TEX<sub>86</sub> ratio is further explored below (section 3.4).

473

474 The second mechanism is that subsurface microbial communities donate enough core  
475 GDGTs to overprint the detrital signal source. The RI (Figure 4B) values were similarly  
476 compared to recorded porewater temperatures to better interpret the TEX<sub>86</sub> trends and to  
477 ensure that the Cathedral Hill reconstructed temperatures are influenced by the subsurface  
478 microbial community. In this regard, RI is used to monitor the adaptive response of an  
479 archaeal community at the hydrothermal vent site. Lipid cyclization is an adaptive response  
480 to changing environmental temperature or acidity in which an archaeon increases its  
481 rigidity by decreasing the fluidity and permeability of its cellular membrane that, therefore,  
482 also further regulates the flow of solutes and nutrients in and out of the cell (Gliozzi et al.,  
483 1983; De Rosa and Gambacorta, 1988; Uda et al., 2001; Schouten et al., 2002; Macalady  
484 et al., 2004; Boyd et al., 2013). Both cores 1 and 2 have RI values highly correlated to  
485 temperature ( $R^2 = 0.87$  and  $0.75$ , respectively) consistent with heat stress adaption. As such,  
486 a significant proportion of the measured *i*GDGTs likely emanate from archaeal  
487 communities living in the shallow sediments of Cathedral Hill. In this regard, the lipid  
488 cyclization pattern may reflect stratigraphically discrete thermophilic to hyperthermophilic  
489 communities that are selectively adapted to more extreme temperature conditions.

490

491

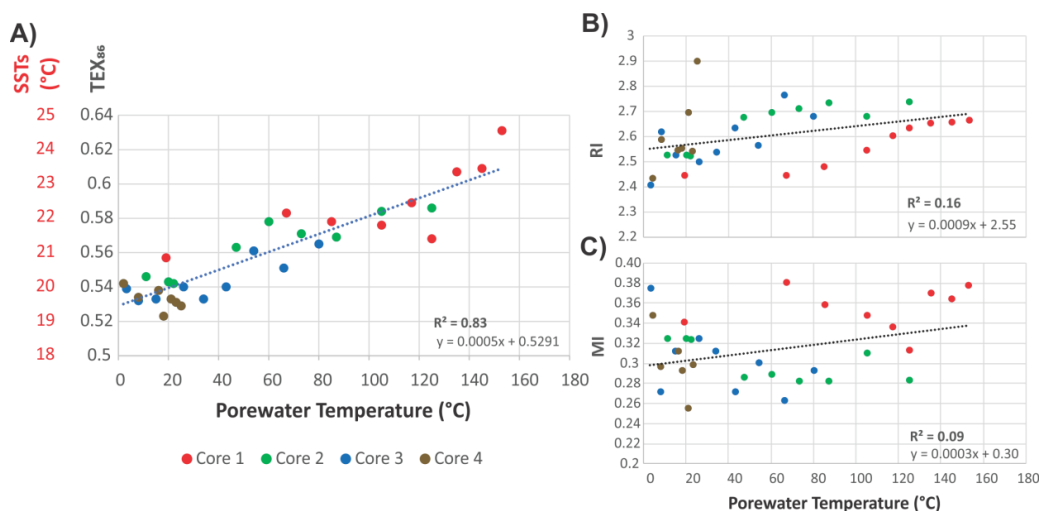


**FIGURE 4.** Cross plots of A) TEX<sub>86</sub>, B) RI, and C) MI, *i*GDGT proxies versus porewater temperature. TEX<sub>86</sub><sup>H</sup> reconstructed MASSTs are based on Kim et al. (2010).

### 492 3.3. Lipid signal sourcing

493 To evaluate the sources of measured archaeal lipids, core and <sub>IPL</sub>TEX<sub>86</sub> indices were  
494 compared as signal response loadings from their respective pools of living and dead cellular

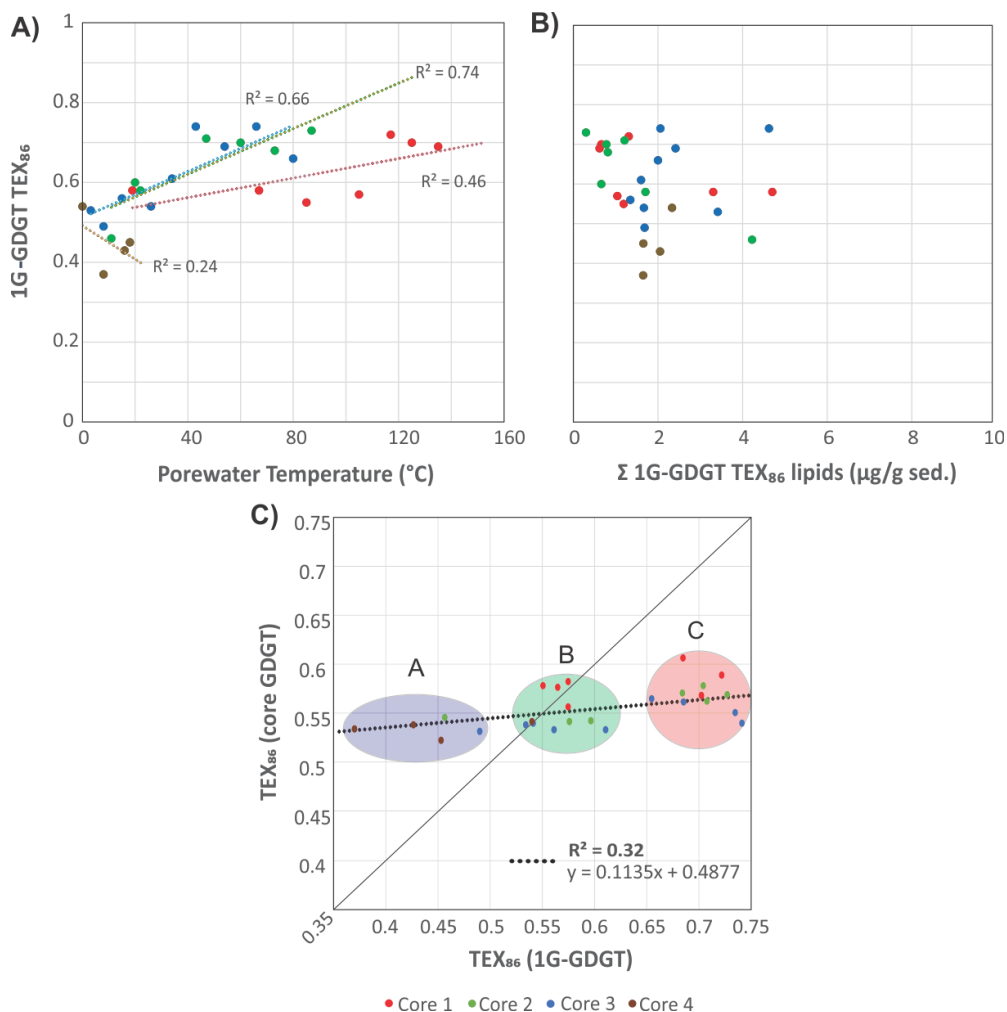


495 debris (Figure 5). For cores 1, 2, and 3 the 1G-*i*GDGT IPLTEX<sub>86</sub> measures are correlated  
496 with temperature ( $R^2 = 0.46, 0.74, \text{ and } 0.66$ , respectively; Figure 5A). In this regard, 1G-  
497 *i*GDGT IPLTEX<sub>86</sub> ratio appears to also measure *in situ* porewater temperatures. Factors  
498 such as community composition and adaptation may further impact the IPLTEX<sub>86</sub> ratio as  
499 the rates of changes between cores 1–3 are not the same. Similar to the CL TEX<sub>86</sub> values,  
500 the IPLTEX<sub>86</sub> are not correlated to their summed TEX<sub>86</sub> lipid abundances (Figure 5B). Such  
501 a condition is consistent with the living lipid pool being modified by the archaeal  
502 community's response to thermal stress and not by subsequent thermal oxidative  
503 transformation occurring shortly after cell death.

504  
505 The IPL and CL lipids of transect samples can be further grouped into three clusters (A, B,  
506 C), suggesting a mixed signal for the sourcing of archaeal GDGTs from both the living and  
507 dead pools of archaea (Figure 5C). In this plot, we assume that clusters falling on the 1:1  
508 line indicate the living biota can equally contribute to the dead pool of total recovered  
509 GDGTs. Those off-axis contribute either less or more to one or the other lipid pool. The  
510 three clusters mark unique thermal zones within the transect area with cluster A being  
511 composed of the ambient core 2 to 4 seafloor surface samples; cluster B marking a mix of  
512 intermediate temperature samples from all cores; and cluster C being composed of high  
513 temperatures samples. The lipid groups likely mark distinct archaeal communities. As  
514 cluster B resides on the 1:1 line, the TEX<sub>86</sub> core lipids likely have a mixed of detrital and  
515 *in situ* inputs. Cluster C, however, appears likely dominated by *in situ* lipid production. The  
516 hyperthermophilic *Methanopyrus kandleri*, recovered from other Guaymas Basin sites  
517 (Teske et al., 2014), may represent one such archaeon contributing to the cluster C lipid  
518 pool. The thermal zonation and equivalent directionality of the resulting ratios (i.e. both CL  
519 and IPL TEX<sub>86</sub> ratios increase with porewater temperature) further supports overprinting  
520 of the original CL TEX<sub>86</sub> sea surface signal by the ocean bottom sediment archaeal  
521 community as a mechanism for the observed CL TEX<sub>86</sub> trends.

522  
523 Collectively, these results suggest the source of the archaeal core lipids measured in the  
524 TEX<sub>86</sub> and RI indices progressively become more dominated by subsurface microbial  
525 communities adapted to the hotter hydrothermal vent fluids. Our results also indicate that  
526 in select natural environments, such as hydrothermal vent complexes, the TEX<sub>86</sub> SST-proxy  
527 may entirely record ocean bottom sediment porewater temperatures. To our knowledge, a  
528 clear case of overprinting to this level has not yet been demonstrated.

529  
530



531

**FIGURE 5.** Cross plots of 1G-*i*GDGTs  $IPLTEX_{86}$  versus (A) porewater temperatures and (B) the concentration of 1G-*i*GDGTs in the sediments. (C)  $TEX_{86}$  proxy of core GDGTs vs 1G-GDGTs. Clusters A–C may represent different archeal communities that are providing varying inputs of *i*GDGT to the core GDGT lipid pool. The dotted trendline is the partial least square regression of the complete core lipid  $TEX_{86}$  data set. The solid line marks the 1:1 CL to IPL proxy correspondance indicating both allochthonous and autochthonous sources contribute equally to the core GDGT lipid pool.

532  
 533  
 534



535 **3.4. TEX<sub>86</sub> overprint corrections**

536 The measured TEX<sub>86</sub> (*M*TEX<sub>86</sub>) value of the Cathedral Hill sediments is herein considered  
 537 to be a weighted sum of a sea surface TEX<sub>86</sub> (*SS*TEX<sub>86</sub>) value acquired from lipids sourced  
 538 in the upper water column that is further modified by a component of water column sourced  
 539 core lipids (*wc*TEX<sub>86</sub>) as well as by additions of archaeal lipids from the benthic and  
 540 subsurface microbial communities (*Sed*TEX<sub>86</sub>). These ratio loadings are potentially further  
 541 modified by diagenetic influences in the ocean bottom sediments. Over the cumulative  
 542 sediment burial period and measured porewater temperatures of the Cathedral Hill push  
 543 core sediments, these influences include the selective loss of lipids by their binding into  
 544 protokerogen (*K*) and potential changes due to the loss of lipid by turnover ( $\varphi$ ; section 3.1).  
 545 Additional catagenetic effects from thermochemical alteration of lipids ( $\theta$ ) may also  
 546 attenuate the sum of sedimentary core lipids by their exposure to high temperature vent  
 547 fluids. Collectively, these effects are considered to form the following relationship:  
 548

$$549 \quad {}_M\text{TEX}_{86} = \frac{a_{SS}\text{TEX}_{86} + b_{wc}\text{TEX}_{86} + c(d_{0-n})_{Sed}\text{TEX}_{86}}{\varphi + K + \theta} \quad (7)$$

551 where *a*, *b*, and *c*, are measured scaling parameters for lipid loading and  $\varphi$ , *K*, and  $\theta$  are  
 552 diagenetic and catagenetic alteration parameters. Solving for *SS*TEX<sub>86</sub>:

$$553 \quad {}_{SS}\text{TEX}_{86} = \frac{{}_M\text{TEX}_{86}(\varphi + K + \theta)}{a} - \frac{b_{wc}\text{TEX}_{86} + c(d_{0-n})_{Sed}\text{TEX}_{86}}{a} \quad (8)$$

556 In this regard, a portion of the archaeal community from the deeper water column,  
 557 presumably initially sourced of IPLs, and an additional community inhabiting the ocean  
 558 floor sediments are assumed to eventually die with their respective IPLs gradually  
 559 becoming converted to CLs that further contribute to the observed *M*TEX<sub>86</sub> value. For this  
 560 study, no data were collected to calculate *b<sub>wc</sub>*TEX<sub>86</sub> and its potential impact on *M*TEX<sub>86</sub>  
 561 is not further considered. However, it is highly likely, given the longer residence times for  
 562 glycosidic-based headgroups of the identified archaeal IPLs and their relatively short  
 563 settling time through the water column that a component of this lipid source could already  
 564 be mixed with the *Sed*TEX<sub>86</sub> value (Lengger et al., 2012). For this study, *Sed*TEX<sub>86</sub> is an IPL-  
 565 TEX<sub>86</sub> ratio based on detected 1G-GDGT-1, -2, -3, and Cren' as present in the original  
 566 paleoclimate proxy (Eq. 1; Table 1; Figure 6). The 2G-GDGT lipids are excluded from the  
 567 calculation due to their low absolute concentrations (<2 μg/g sed.), their limited number of  
 568 detected TEX<sub>86</sub> core lipid configurations (comprising only of GDGT-1 and GDGT-2; Table  
 569 A2), and their short stratigraphic zones of occurrence (section 3.1). The *Sed*TEX<sub>86</sub> is further  
 570 scaled by the summed concentrations of these lipids as they increasingly accumulate with  
 571 sediment depth (*d<sub>0-n</sub>*). For Cathedral Hill, the sum of allochthonous TEX<sub>86</sub> lipids ( $\Sigma[\text{GDGTs}$   
 572 *CL-TEX<sub>86</sub> lipids]<sub>0-2</sub>) is estimated to be 120 μg/g sed. based on an average surface lipid  
 573 concentration (0-2 cmbsf) measured across the four core transect. As such,  
 574*

$$575 \quad c(d_{0-n}) = \sum_{i=0}^n \left( \frac{[\text{GDGTs}_{IPL-TEX_{86} \text{ lipids}}]_n}{[\text{GDGTs}_{CL-TEX_{86} \text{ lipids}}]_{0-2cm}} \right) \quad (9)$$

576  
577



577 where  $n$  is the deepest point of sediment burial.

578

579 Selective lipid removal by diagenetic and catagenetic processes theoretically may also affect  
 580 the  $\text{TEX}_{86}$  value; however, their perspective impact on the directionality and magnitude of  
 581 the ratio are difficult to predict and equally hard to discretely measure. For Cathedral Hill,  
 582 although the loss of GDGTs to protokerogen formation could potentially impact the ratio,  
 583 it has been proven to be very low for the analyzed sediments (Bentley et al., 2021). As such,  
 584 the selectivity of lipid classes being adsorbed to a protokerogen is undeterminable. More  
 585 importantly, for this site it is insignificant, and the  $K$  parameter in Eqs. 7 and 8 is therefore  
 586 assigned a value of 0.

587

588 The degradation rates of each  $\text{TEX}_{86}$  lipid class were independently measured for the four  
 589 push cores (Eq. 6; Fig. A2). Given the high geothermal gradient at Cathedral Hill, some of  
 590 the transect push core sediments resided within zones of active catagenesis (Fig. 2; Dalzell  
 591 et al., 2021). As the abundance of both CLs and IPLs differentially decreases through the  
 592 various core sediment profiles with turnover rates that appear to be constrained by  
 593 porewater temperature changes (section 3.1), the degradation rates must also record the  
 594 effects of thermochemical oxidative weathering (Fig. 3B). In this case,  $\varphi$  and  $\theta$  are  
 595 therefore treated as a grouped parameter.

596

597 To determine if individual lipid classes were selectively removed during degradation, the  
 598 variance ( $s^2$ ) of the rate change as measured from its respective regression slope (i.e.  $m_{\log k'}$ )  
 599 of the  $\text{TEX}_{86}$  lipid classes (Fig. A2; Supplemental Table A3 from Eq. 6) were calculated.  
 600 For the Cathedral Hill transect, the calculated  $m_{\log k'} s^2$  is 0.11, which suggests near equal  
 601 degradation rates for all  $\text{TEX}_{86}$  lipid classes. Therefore, lipid turnover and the concomitant  
 602 thermochemical oxidation of these lipid classes is also similarly non-selective. A weighing  
 603 function for the degree of lipid class selectivity during turnover is nonetheless proposed:

604

$$605 \quad \varphi + \theta = 1/M\text{TEX}_{86}^{0.11} \quad (10)$$

606

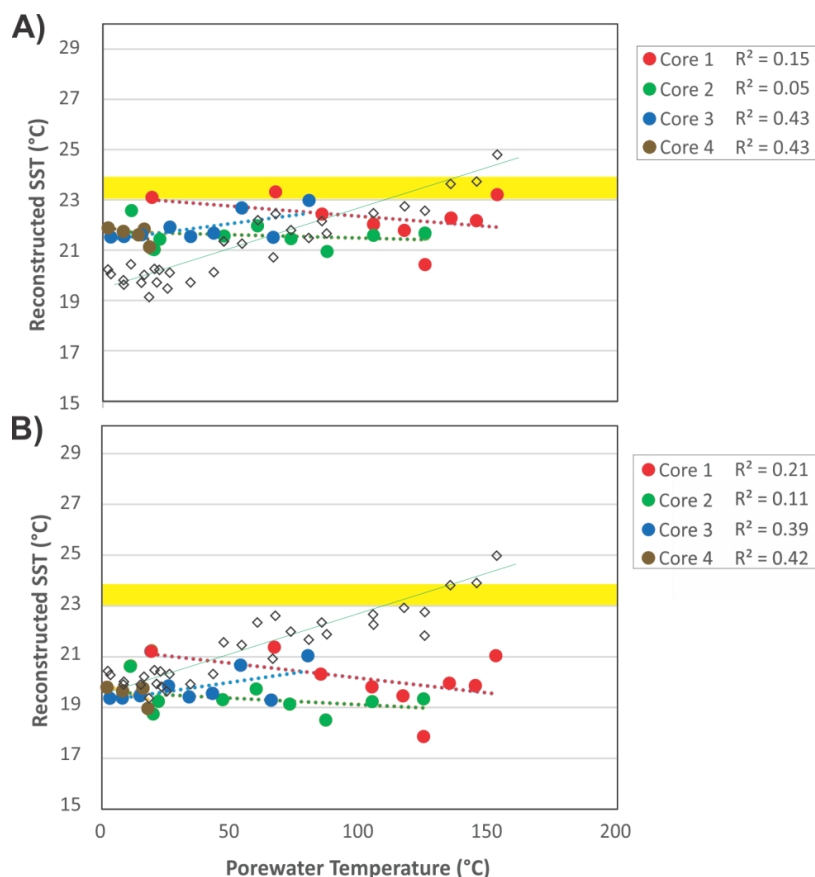
607 When applied to Eq. 8 minor changes to the reconstructed lumped  $_{SS+WC}\text{TEX}_{86}$  ratio are  
 608 observed consistent with the absence of a comparative relationship between  $i$ GDGT down  
 609 core lipid depletions and the respective  $M\text{TEX}_{86}$  ratios across the biologically active zone  
 610 of the transect sediments (section 3.1; Figure 3B).

611

612 Equation 7 predicts an average transect  $_{SS+WC}\text{TEX}_{86}^H$  reconstructed SST of  $21.92 \pm 0.66$  °C  
 613 with no elevated trends for increasing porewater temperatures across each of the transect  
 614 cores (Table 2; Figure 6A). If the  $\varphi$ ,  $K$ , and  $\theta$  scaling parameters are removed from the  
 615 calculation the average temperature shifts 2.08 °C lower to  $19.69 \pm 0.39$  °C (Table 2; Figure  
 616 6B). The marginal change is likely due to only a few sediment samples displaying evidence  
 617 of *in situ* hydrocarbon generation associated with thermochemical oxidation (Dalzell et al.,  
 618 2021). Irrespective of approach, but particularly the case for the more simplified  
 619 expression, all measures produce values closer to the expected SST of 19.3–20.4 °C that is  
 620 based on the range of values recorded for core 4 and the three transect surface sediments  
 621 (section 3.2). These values are  $\sim 3$  °C lower than the 23–24 °C obtained for the 21-year  
 622 (1982–2004) satellite-derived MASST data for the Guaymas Basin region (Herrera-



623 Cervantes et al., 2007). Nonetheless, nearly all  $MTEX_{86}$  attenuation can therefore be  
624 attributed to sediment microbial overprinting. The high degree of influence is striking given  
625 that the upper water flux of GDGTs is estimated to represents up to 93% of the total intact  
626 polar and core GDGT lipid pool within these sediments. In this regard, it demonstrated that  
627 microbial community influences  $TEX_{86}$  measurements.  
628  
629



630  
631  
632  
633 **FIGURE 6.** Reconstructed  $ssTEX_{86}$  SSTs from (A) Eq. 8 and (B) Eq. 8 without  $\phi$ ,  $K$ , and  
634  $\theta$  scaling parameters compared to measured porewater temperatures.  $MTEX_{86}$  values are  
635 also plotted for reference (open green circles). Yellow field is the 23–24 °C range observed  
636 for the 21-year (1982–2004) satellite-derived MASST data (Herrera-Cervantes et al.,  
637 2007). The corrected data series show a lack of correlation suggesting that model can back-  
638 out the original SST signal.  
639



640  
 641 **Table 2.** Reconstructed sea surface temperatures.  
 642

Sample	Depth (cmbsf)	Porewater Temp. (°C)	<i>t</i> Time (yrs.)	$M$ TEX <sub>86</sub> (Measured iGDGT TEX <sub>86</sub> )	Reconstructed SST (°C)	TEX <sub>86</sub> 1G-GDGT IPLs (µg/g)	Cumulative 1G-GDGTs Loading with Depth (µg/g)	$S_{66}$ TEX <sub>86</sub> (i.e. 1G-GDGT IPLTEX <sub>86</sub> )	<i>c</i> ( <i>d<sub>0-n</sub></i> ) Cumulative Weighted IPL Loading (Eq. 9)
Core 1 (0-2cm)	1	19	10	0.56	21.2	4.80	0	0.58	0.00
Core 1 (2-4cm)	3	67	20	0.58	22.6	3.41	4.80	0.58	0.04
Core 1 (4-6cm)	5	85	30	0.58	22.3	1.29	8.21	0.55	0.07
Core 1 (6-8cm)	7	105	40	0.58	22.2	1.14	9.50	0.57	0.08
Core 1 (8-10cm)	9	117	50	0.59	22.9	1.41	10.64	0.72	0.09
Core 1 (10-12cm)	11	125	60	0.57	21.8	0.76	12.05	0.70	0.10
Core 1 (12-15cm)	13	135	70	0.61	23.8	0.72	12.81	0.69	0.11
Core 1 (15-18cm)	17	145	80	0.61	23.9	0.00	13.53	0.69	0.11
Core 1 (18-21cm)	20	153	90	0.63	24.9	0.00	13.53	0.69	0.11
<b>Avg.</b>				<b>0.59</b>	<b>22.84</b>				
<b>Std. Dev.</b>				<b>0.02</b>	<b>1.16</b>				
Core 2 (0-2cm)	1	11	10	0.55	20.6	4.33	0	0.46	0.00
Core 2 (2-4cm)	3	22	20	0.54	20.4	1.80	4.33	0.58	0.04
Core 2 (4-6cm)	5	20	30	0.54	20.5	0.76	6.13	0.60	0.05
Core 2 (6-8cm)	7	47	40	0.56	21.5	1.31	6.89	0.71	0.06
Core 2 (8-10cm)	9	60	50	0.58	22.3	0.88	8.20	0.70	0.07
Core 2 (10-12cm)	11	73	60	0.57	22.0	0.92	9.08	0.68	0.08
Core 2 (12-15cm)	13	87	70	0.57	21.8	0.40	10.00	0.73	0.08
Core 2 (15-18cm)	17	105	80	0.58	22.6	0.00	10.40	0.73	0.09
Core 2 (18-21cm)	20	125	90	0.59	22.7	0.00	10.40	0.73	0.09
<b>Avg.</b>				<b>0.56</b>	<b>21.61</b>				
<b>Std. Dev.</b>				<b>0.02</b>	<b>0.91</b>				
Core 3 (0-2cm)	1	3.2	10	0.54	20.2	3.51	0	0.53	0.03
Core 3 (2-4cm)	3	8	20	0.53	19.9	1.79	3.51	0.49	0.01
Core 3 (4-6cm)	5	15	30	0.53	19.9	1.45	5.30	0.56	0.01
Core 3 (6-8cm)	7	26	40	0.54	20.3	1.77	6.74	0.54	0.01
Core 3 (8-10cm)	9	34	50	0.53	19.9	1.70	8.51	0.61	0.01
Core 3 (10-12cm)	11	43	60	0.54	20.3	2.16	10.21	0.74	0.02
Core 3 (12-15cm)	13	54	70	0.56	21.4	2.52	12.37	0.69	0.02
Core 3 (15-18cm)	17	66	80	0.55	20.9	4.72	14.89	0.74	0.04
Core3 (18-21cm)	20	80	90	0.57	21.6	2.10	19.61	0.66	0.02



<b>Avg.</b>				<b>0.54</b>	<b>20.50</b>				
<b>Std. Dev.</b>				<b>0.01</b>	<b>0.67</b>				
Core 4 (0-2cm)	1	2	10	0.54	20.4	2.43	0	0.54	0.02
Core 4 (2-4cm)	3	8	20	0.53	20.0	1.75	2.43	0.37	0.01
Core 4 (4-6cm)	5	16	30	0.54	20.2	2.15	4.18	0.43	0.02
Core 4 (6-8cm)	7	18	40	0.52	19.3	1.76	6.34	0.45	0.01
Core 4 (8-10cm)	9	21	50	0.53	19.9	0.44	8.09	-	-
Core 4 (10-12cm)	11	23	60	0.53	19.8	2.20	8.54	-	-
Core 4 (12-15cm)	13	25	70	0.53	19.7	0.00	10.74	-	-
<b>Avg.</b>				<b>0.53</b>	<b>19.90</b>				
<b>Std. Dev.</b>				<b>0.01</b>	<b>0.34</b>				
<b>Avg.</b>									
<b>Std. Dev.</b>									



**Table 2.** Reconstructed sea surface temperatures (continued).

Sample	Eq. 8 excluding $\phi+\theta+K$			Eq. 8 including $\phi+\theta+K$		
	$SS+WC\text{TEX}_{86} (M\text{TEX}_{86} - c(d_{0-n})^*_{sed}\text{TEX}_{86})$	$SS+WC\text{TEX}_{86}^H$ (after Kim et al., 2010)	$SS+WC\text{TEX}_{86}^H$ Reconstructed SST ( $^{\circ}\text{C}$ )	$\phi+\theta$ (Eq. 10) (where $s^2 = 0.11$ ; Table A3)	$SS+WC\text{TEX}_{86}$	$SS+WC\text{TEX}_{86}^H$ Reconstructed SST ( $^{\circ}\text{C}$ ) (after Kim et al., 2010)
Core 1 (0-2cm)	0.56	-0.25	21.2	1.07	0.59	23.1
Core 1 (2-4cm)	0.56	-0.25	21.4	1.07	0.60	23.3
Core 1 (4-6cm)	0.54	-0.27	20.3	1.07	0.58	22.5
Core 1 (6-8cm)	0.53	-0.27	19.8	1.07	0.57	22.0
Core 1 (8-10cm)	0.52	-0.28	19.5	1.07	0.57	21.8
Core 1 (10-12cm)	0.50	-0.30	17.9	1.08	0.54	20.5
Core 1 (12-15cm)	0.53	-0.27	20.0	1.07	0.58	22.3
Core 1 (15-18cm)	0.53	-0.27	19.8	1.07	0.58	22.2
Core 1 (18-21cm)	0.55	-0.26	21.0	1.07	0.60	23.2
<b>Avg.</b>	<b>0.54</b>	<b>-0.27</b>	<b>20.10</b>	<b>1.07</b>	<b>0.58</b>	<b>22.33</b>
<b>Std. Dev.</b>	<b>0.02</b>	<b>0.02</b>	<b>1.08</b>	<b>0.00</b>	<b>0.02</b>	<b>0.89</b>
Core 2 (0-2cm)	0.55	-0.26	20.6	1.07	0.58	22.6
Core 2 (2-4cm)	0.52	-0.28	19.2	1.07	0.56	21.5
Core 2 (4-6cm)	0.51	-0.29	18.7	1.08	0.55	21.1
Core 2 (6-8cm)	0.52	-0.28	19.3	1.07	0.56	21.6
Core 2 (8-10cm)	0.53	-0.28	19.7	1.07	0.57	22.0
Core 2 (10-12cm)	0.52	-0.28	19.1	1.07	0.56	21.5
Core 2 (12-15cm)	0.51	-0.29	18.5	1.08	0.55	21.0
Core 2 (15-18cm)	0.52	-0.28	19.2	1.07	0.56	21.6
Core 2 (18-21cm)	0.52	-0.28	19.3	1.07	0.57	21.7
<b>Avg.</b>	<b>0.52</b>	<b>-0.28</b>	<b>19.32</b>	<b>1.07</b>	<b>0.56</b>	<b>21.61</b>
<b>Std. Dev.</b>	<b>0.01</b>	<b>0.01</b>	<b>0.60</b>	<b>0.00</b>	<b>0.01</b>	<b>0.49</b>
Core 3 (0-2cm)	0.52	-0.28	19.4	1.07	0.56	21.5
Core 3 (2-4cm)	0.52	-0.28	19.4	1.07	0.56	21.6
Core 3 (4-6cm)	0.53	-0.28	19.5	1.07	0.57	21.7
Core 3 (6-8cm)	0.53	-0.27	19.9	1.07	0.57	21.9
Core 3 (8-10cm)	0.52	-0.28	19.4	1.07	0.56	21.6
Core 3 (10-12cm)	0.53	-0.28	19.6	1.07	0.57	21.7
Core 3 (12-15cm)	0.55	-0.26	20.7	1.07	0.59	22.7
Core 3 (15-18cm)	0.52	-0.28	19.3	1.07	0.56	21.5
Core3 (18-21cm)	0.55	-0.26	21.0	1.07	0.59	23.0
<b>Avg.</b>	<b>0.53</b>	<b>-0.27</b>	<b>19.79</b>	<b>1.07</b>	<b>0.57</b>	<b>21.91</b>
<b>Std. Dev.</b>	<b>0.01</b>	<b>0.01</b>	<b>0.62</b>	<b>0.00</b>	<b>0.01</b>	<b>0.55</b>
Core 4 (0-2cm)	0.53	-0.27	19.8	1.07	0.57	21.9
Core 4 (2-4cm)	0.53	-0.28	19.7	1.07	0.57	21.8



Core 4 (4-6cm)	0.53	-0.28	19.8	1.07	0.57	21.9
Core 4 (6-8cm)	0.52	-0.29	19.0	1.08	0.56	21.2
Core 4 (8-10cm)	-	-	-			
Core 4 (10-12cm)	-	-	-			
Core 4 (12-15cm)	-	-	-			
<b>Avg.</b>	<b>0.53</b>	<b>-0.28</b>	<b>19.55</b>	<b>1.07</b>	<b>0.65</b>	<b>21.67</b>
<b>Std. Dev.</b>	<b>0.01</b>	<b>0.01</b>	<b>0.39</b>	<b>0.00</b>	<b>0.01</b>	<b>0.35</b>
			<b>19.71</b>			<b>21.92</b>
			<b>0.79</b>			<b>0.66</b>

643

644

#### 645 **4. Conclusions**

646 For this study, we demonstrate the commonly used TEX<sub>86</sub> paleoclimate proxy can become  
647 heavily impacted by the ocean floor archaeal community. For the Cathedral Hill vent site  
648 at Guaymas Basin, the lipids sourced from these sediments resulted in TEX<sub>86</sub> reconstructed  
649 temperatures that record conditions of the advecting porewaters. However, the impact  
650 appears to result from a combination of source inputs, their diagenetic and catagenetic  
651 alteration, and further overprint by the additions of lipids from the ocean floor sedimentary  
652 archaeal community that has adapted to the high-temperature conditions of the vent fluids  
653 by producing more cyclized ring moieties to rigidify their cellular membranes. Together,  
654 these processes resulted in absolute TEX<sub>86</sub><sup>H</sup> temperature offsets of up to 4 °C based on  
655 calibrations closely suited to the latitudinal position of Guaymas Basin. Such large offsets  
656 could be meaningful to paleoclimate reconstructions (i.e. global changes by 2–4 °C mean  
657 completed deglaciation). As such, we further present a method to correct the overprints by  
658 both water column and subsurface archaeal community's using IPLs extracted from both  
659 of these sources. Although, we have not been able to test this model with lipid inputs from  
660 the overlying water column, we have demonstrated its effectiveness at removing sediment  
661 sourced overprints, which may not be unique to hydrothermal systems. This approach  
662 should be capable of being extended to all near-surface marine sediment systems and may  
663 improve the quality of calibration models or climate reconstructions that are based on  
664 TEX<sub>86</sub> measures.

665

666

667

#### 668 **Conflicts of Interest**

669 The authors declare no conflict of interest.

670

#### 671 **Supplementary information**

672 Supplementary material related to this article can be found on-line at <https://doi.org/.....>



673 **References**

- 674 Bentley, J. N., Ventura, G. T., Dalzell, C. J., Walters, C. C., Peters, C. A., Mennito, A. S.,  
675 Nelson, R. K., Reddy, C. M., Walters, C. J., Seewald, J., & Sievert, S. M. (2021).  
676 Archaeal lipid diversity, alteration, preservation at Cathedral Hill, Guaymas Basin,  
677 and its link to the deep time preservation paradox. *Organic Geochemistry*. Accepted  
678 with revision.  
679
- 680 Biddle, J. F., Cardman, Z., Mendlovitz, H., Albert, D. B., Lloyd, K. G., Boetius, A., &  
681 Teske, A. (2012). Anaerobic oxidation of methane at different temperature regimes  
682 in Guaymas Basin hydrothermal sediments. *ISME Journal* 6, 1018–1031.  
683 <http://dx.doi.org/10.1038/ismej.2011.164>.  
684
- 685 Boyd, E., Hamilton, T., Wang, J., He, L., & Zhang, C. (2013). The role of tetraether lipid  
686 composition in the adaptation of thermophilic archaea to acidity. *Frontiers in*  
687 *microbiology*, 4, 62.  
688
- 689 Brassell, S. C., Eglinton, G., Marlowe, I. T., Pflaumann, U., & Sarnthein, M. (1986).  
690 Molecular stratigraphy: a new tool for climatic assessment. *Nature*, 320, 129–133.  
691
- 692 Calvert, S. E. (1966). Origin of diatom-rich, varved sediments from the Gulf of  
693 California. *The Journal of Geology*, 74, 546–565.  
694
- 695 Curray, J. R., Moore, D. G., Lawver, L. A., Emmel, F. J., Raitt, R. W., Henry, M., &  
696 Kieckhefer, R. (1979). Tectonics of the Andaman Sea and Burma: convergent  
697 margins. In J.S. Watkins, L. Montadert, P.W. Dickerson (Eds.) *Geological and*  
698 *Geophysical Investigations of Continental Margins*, AAPG Memoir 29, 189–198.  
699
- 700 Dalzell, C. J., Ventura, G. T., Nelson, R. K., Reddy, C. M., Walters, C. J., Seewald, J., &  
701 Sievert, S. M. (2021). Resolution of multi-molecular hydrocarbon transformation in  
702 petroleum-bearing sediments from the Cathedral Hill hydrothermal vent complex at  
703 Guaymas Basin, Gulf of California by comprehensive two-dimensional gas  
704 chromatography and chemometric analyses. *Journal: Organic Geochemistry*, 152,  
705 104173.  
706
- 707 De Rosa, M., & Gambacorta, A. (1988). The lipids of archaebacteria. *Progress in lipid*  
708 *research*, 27, 153–175.  
709
- 710 Elling, F. J., Könneke, M., Mußmann, M., Greve, A., & Hinrichs, K. U. (2015). Influence  
711 of temperature, pH, and salinity on membrane lipid composition and TEX<sub>86</sub> of  
712 marine planktonic thaumarchaeal isolates. *Geochimica et Cosmochimica Acta*, 171,  
713 238–255.  
714
- 715 Gieskes, J. M., Simoneit, B. R., Brown, T., Shaw, T. J., Wang, Y. C., & Magenheim, A.  
716 (1988). Hydrothermal fluids and petroleum in surface sediments of Guaymas Basin,  
717 Gulf of California: a case study. *The Canadian Mineralogist*, 26, 589–602.  
718



- 719 Gliozzi, A., Paoli, G., De Rosa, M., & Gambacorta, A. (1983). Effect of isoprenoid  
720 cyclization on the transition temperature of lipids in thermophilic  
721 archaeobacteria. *Biochimica et Biophysica Acta (BBA)-Biomembranes*, 735, 234–  
722 242.  
723
- 724 Ho, S. L. & Laepple, T. (2016). Flat meridional temperature gradient in the early Eocene  
725 in the subsurface rather than surface ocean. *Nature Geoscience*, 9, 606–610.  
726
- 727 Hollis, C.J., Taylor, K.W.R., Handley, L., Pancost, R.D., Huber, M., Creech, J.B., Hines,  
728 B.R., Crouch, E.M., Morgans, H.E.G., Crampton, J.S., Gibbs, S., Pearson, P.N., &  
729 Zachos, J.C. (2012). Early Paleogene temperature history of the Southwest Pacific  
730 Ocean: Reconciling proxies and models. *Earth and Planetary Science Letters* 349–  
731 350, 53–66  
732
- 733 Hopmans, E. C., Weijers, J. W., Schefuß, E., Herfort, L., Sinninghe Damsté, J. S., &  
734 Schouten, S. (2004). A novel proxy for terrestrial organic matter in sediments based  
735 on branched and isoprenoid tetraether lipids. *Earth and Planetary Science*  
736 *Letters*, 224, 107–116.  
737
- 738 Huguet, C., Cartes, J. E., Sinninghe Damsté, J. S., & Schouten, S. (2006). Marine  
739 crenarchaeotal membrane lipids in decapods: Implications for the TEX<sub>86</sub>  
740 paleothermometer. *Geochemistry, Geophysics, Geosystems*, 7. doi  
741 10.1029/2006GC001305.  
742
- 743 Huguet, C., Schimmelmann, A., Thunell, R., Lourens, L. J., Sinninghe Damsté, J. S., &  
744 Schouten, S. (2007). A study of the TEX<sub>86</sub> paleothermometer in the water column  
745 and sediments of the Santa Barbara Basin, California. *Paleoceanography*, 22, doi  
746 10.1029/2006PA001310.  
747
- 748 Hurley, S.J., Elling, F.J., Könneke, M., Buchwald, C., Wankel, S.D., Santoro, A.E., Lipp,  
749 J.S., Hinrichs, K.-U., Pearson, A., 2016. Influence of ammonia oxidation rate on  
750 thaumarchaeal lipid composition and the TEX<sub>86</sub> temperature proxy. *Proceedings of*  
751 *the National Academy of Sciences*, 113, 7762-7767.  
752
- 753 Kashefi, K., & Lovley, D. R. (2003). Extending the upper temperature limit for  
754 life. *Science*, 301, 934–934.  
755
- 756 Kim, J. H., Schouten, S., Hopmans, E. C., Donner, B., & Damsté, J. S. S. (2008). Global  
757 sediment core-top calibration of the TEX<sub>86</sub> paleothermometer in the  
758 ocean. *Geochimica et Cosmochimica Acta*, 72, 1154–1173.  
759
- 760 Kim, J. H., Van der Meer, J., Schouten, S., Helmke, P., Willmott, V., Sangiorgi, F., Koç,  
761 N., Hopmans, E. C. & Damsté, J. S. S. (2010). New indices and calibrations derived  
762 from the distribution of crenarchaeal isoprenoid tetraether lipids: Implications for  
763 past sea surface temperature reconstructions. *Geochimica et Cosmochimica Acta*, 74,  
764 4639–4654.  
765



- 766 Kim J.-H., Romero O. E., Lohmann G., Donner B., Laepple T., Haam E. & Sinninghe  
767 Damsté J. S. (2012a) Pronounced subsurface cooling of North Atlantic waters off  
768 Northwest Africa during Dansgaard-Oeschger interstadials. *Earth and Planetary*  
769 *Science Letters*, 339–340, 95–102.  
770
- 771 Kim, J. H., Crosta, X., Willmott, V., Renssen, H., Bonnin, J., Helmke, P., Schouten, S. &  
772 Sinninghe Damsté, J. S. (2012b). Holocene subsurface temperature variability in the  
773 eastern Antarctic continental margin. *Geophysical Research Letters*, 39. doi  
774 10.1029/2012GL051157.  
775
- 776 Kim J.-H., Schouten, S., Rodrigo-Gamiz, M., Rampen, S., Marino, G., Huguet, C.,  
777 Helmke, P., Buscail, R., Hopmans, E. C., Pross, J., Sangiorgi, F., Middelburg, J. B.  
778 M., & Sinninghe Damsté J. S. (2015). Influence of deep-water derived isoprenoid  
779 tetraether lipids on the paleothermometer in the Mediterranean Sea. *Geochimica et*  
780 *Cosmochimica Acta*, 150, 125–141.  
781
- 782 Knappy, C. S., Chong, J. P., & Keely, B. J. (2009). Rapid discrimination of archaeal  
783 tetraether lipid cores by liquid chromatography-tandem mass spectrometry. *Journal*  
784 *of the American Society for Mass Spectrometry*, 20, 51–59.  
785
- 786 Lawrence, K. T., Pearson, A., Castaneda, I. S., Ladlow, C., Peterson, L. C., Lawrence, G.  
787 E. (2020). Comparison of Late Neogene  $U^{k}_{37}$  and  $TEX_{86}$  Paleotemperature records  
788 from the eastern equatorial Pacific at orbital resolution. *Paleoceanography and*  
789 *Paleoclimatology*, 35, 1–16.  
790
- 791 Lengger, S.K., Hopmans, E.C., Reichart, G.-J., Nierop, K.G.J., Sinninghe Damsté, J.S.,  
792 Schouten, S., 2012. Intact polar and core glycerol dibiphytanyl glycerol tetraether  
793 lipids in the Arabian Sea oxygen minimum zone. Part II: Selective preservation and  
794 degradation in sediments and consequences for the  $TEX_{86}$ . *Geochimica et*  
795 *Cosmochimica Acta* 98, 244–258.  
796
- 797 Liu, X. L., Leider, A., Gillespie, A., Gröger, J., Versteegh, G. J., & Hinrichs, K. U.  
798 (2010). Identification of polar lipid precursors of the ubiquitous branched GDGT  
799 orphan lipids in a peat bog in Northern Germany. *Organic Geochemistry*, 41, 653–  
800 660.  
801
- 802 Liu, X. L., Lipp, J. S., Simpson, J. H., Lin, Y. S., Summons, R. E., & Hinrichs, K. U.  
803 (2012). Mono- and dihydroxyl glycerol dibiphytanyl glycerol tetraethers in marine  
804 sediments: Identification of both core and intact polar lipid forms. *Geochimica et*  
805 *Cosmochimica Acta*, 89, 102–115.  
806
- 807 Liu, X. L., Russell, D. A., Bonfio, C., Summons, R. E. (2018) Glycerol configurations of  
808 environmental GDGTs investigated using a selective sn2 ether cleavage protocol.  
809 *Organic Geochemistry*, 128, 57–62.  
810
- 811 Lipp, J. S., & Hinrichs, K. U. (2009). Structural diversity and fate of intact polar lipids in  
812 marine sediments. *Geochimica et Cosmochimica Acta*, 73, 6816–6833.



- 813  
814 Lipp, J. S., Morono, Y., Inagaki, F., & Hinrichs, K. U. (2008). Significant contribution of  
815 Archaea to extant biomass in marine subsurface sediments. *Nature*, 454, 991–994.  
816  
817 Lonsdale, P., & Becker, K. (1985). Hydrothermal plumes, hot springs, and conductive  
818 heat flow in the Southern Trough of Guaymas Basin. *Earth and Planetary Science  
819 Letters*, 73, 211–225.  
820  
821 Lopes dos Santos R. A., Prange M., Castañeda I. S., Schefuß E., Mulitza S., Schulz M.,  
822 Niedermeyer E. M., Sinninghe Damsté J. S. and Schouten S. (2010). Glacial–  
823 interglacial variability in Atlantic meridional overturning circulation and thermocline  
824 adjustments in the tropical North Atlantic. *Earth and Planetary Science Letters*, 300,  
825 407–414.  
826  
827 Lunt, D. J., Haywood, A. M., Schmidt, G. A., Salzmann, U., Valdes, P. J., Dowsett, H. J.,  
828 & Loptson, C.A. (2012). On the causes of mid-Pliocene warmth and polar  
829 amplification. *Earth and Planetary Science Letters*, 321–322, 128–138,  
830 doi:10.1016/j.epsl.2011.12.042.  
831  
832 Macalady, J. L., Vestling, M. M., Baumler, D., Boekelheide, N., Kaspar, C. W., &  
833 Banfield, J. F. (2004). Tetraether-linked membrane monolayers in *Ferroplasma* spp:  
834 a key to survival in acid. *Extremophiles*, 8, 411–419.  
835  
836 McClymont, E. L., Ganeshram, R. S., Pichevin, L. E., Talbot, H. M., van Dongen, B. E.,  
837 Thunell, R. C., Haywood, A.M., Singarayer, J.S. & Valdes, P. J. (2012). Sea-surface  
838 temperature records of Termination 1 in the Gulf of California: Challenges for  
839 seasonal and interannual analogues of tropical Pacific climate  
840 change. *Paleoceanography*, 27. doi 10.1029/2011PA002226.  
841  
842 McKay, L. J., MacGregor, B. J., Biddle, J. F., Albert, D. B., Mendlovitz, H. P., Hoer, D.  
843 R., Lipp, J.S., Lloyd, K.G & Teske, A. P. (2012). Spatial heterogeneity and  
844 underlying geochemistry of phylogenetically diverse orange and white Beggiatoa  
845 mats in Guaymas Basin hydrothermal sediments. *Deep Sea Research Part I:  
846 Oceanographic Research Papers*, 67, 21–31.  
847  
848 Meyer, S., Wegener, G., Lloyd, K. G., Teske, A., Boetius, A., & Ramette, A. (2013).  
849 Microbial habitat connectivity across spatial scales and hydrothermal temperature  
850 gradients at Guaymas Basin. *Frontiers in Microbiology*, 4, 207.  
851  
852 Moore, D. G. (1973). Plate-edge deformation and crustal growth, Gulf of California  
853 structural province. *Geological Society of America Bulletin*, 84), 1883–1906.  
854  
855 Naafs, B. D. A., Rohrssen, M., Inglis, G. N., Lähteenoja, O., Feakins, S. J., Collinson, M.  
856 E., Kennedy, E.M., Singh, P.K., Singh, M.P., Lunt, D.J., Pancost, R. D. (2018). High  
857 temperatures in the terrestrial mid-latitudes during the early Palaeogene. *Nature  
858 Geoscience*, 11, 766–771.  
859



- 860 Pearson A. and Ingalls A. E. (2013) Assessing the use of archaeal lipids as marine  
861 environmental proxies. *Annual Review Earth Planetary Science*, 41, 15.1–15.26.  
862
- 863 Pearson, A., Huang, Z., Ingalls, A. E., Romanek, C. S., Wiegel, J., Freeman, K. H.,  
864 Smittenberg, R.H. & Zhang, C. L. (2004). Nonmarine crenarchaeol in Nevada hot  
865 springs. *Applied and Environmental Microbiology*, 70, 5229–5237.  
866
- 867 Powers, L., Werne, J. P., Vanderwoude, A. J., Sinninghe Damsté, J. S., Hopmans, E. C.,  
868 & Schouten, S. (2010). Applicability and calibration of the TEX<sub>86</sub> paleothermometer  
869 in lakes. *Organic Geochemistry*, 41, 404–413.  
870
- 871 Qin, W., Carlson, L. T., Armbrust, E. V., Devol, A. H., Moffett, J. W., Stahl, D. A., &  
872 Ingalls, A. E. (2015). Confounding effects of oxygen and temperature on the TEX<sub>86</sub>  
873 signature of marine Thaumarchaeota. *Proceedings of the National Academy of  
874 Sciences*, 112(35), 10,979–10,984. <https://doi.org/10.1073/pnas.1501568112>.  
875
- 876 Schouten, S., Hopmans, E. C., and Sinninghe Damsté, J. S. (2013). The organic  
877 geochemistry of glycerol dialkyl glycerol tetraether lipids: A review. *Organic  
878 Geochemistry*, 54, 19–61.  
879
- 880 Schouten, S., Hopmans, E. C., & Sinninghe Damsté, J. S. (2004). The effect of maturity  
881 and depositional redox conditions on archaeal tetraether lipid  
882 palaeothermometry. *Organic Geochemistry*, 35, 567–571.  
883
- 884 Schouten, S., Hopmans, E. C., Schefuß, E., & Sinninghe Damsté, J. S. (2002).  
885 Distributional variations in marine crenarchaeotal membrane lipids: a new tool for  
886 reconstructing ancient sea water temperatures? *Earth and Planetary Science  
887 Letters*, 204, 265–274.  
888
- 889 Schouten S., Wakeham S. G., Hopmans E. C. and Damsté J. S. S. (2003) Biogeochemical  
890 Evidence that Thermophilic Archaea Mediate the Anaerobic Oxidation of Methane.  
891 *Appl. Environ. Microbiol.* 69, 1680-1686.  
892
- 893 Sinninghe Damsté, J. S. S., Ossebaar, J., Abbas, B., Schouten, S., & Verschuren, D.  
894 (2009). Fluxes and distribution of tetraether lipids in an equatorial African lake:  
895 constraints on the application of the TEX<sub>86</sub> palaeothermometer and BIT index in  
896 lacustrine settings. *Geochimica et Cosmochimica Acta*, 73, 4232–4249.  
897
- 898 Sinninghe Damsté J. S., Rijpstra W. I. C., Hopmans E. C., den Uijl M. J., Weijers J. W.  
899 H. and Schouten S. (2018) The enigmatic structure of the crenarchaeol isomer.  
900 *Organic Geochemistry* 124, 22-28.  
901
- 902 Stadnitskaia, A., Nadezhkin, D., Abbas, B., Blinova, V., Ivanov, M. K., & Sinninghe  
903 Damsté, J. S. (2008). Carbonate formation by anaerobic oxidation of methane:  
904 evidence from lipid biomarker and fossil 16S rDNA. *Geochimica et Cosmochimica  
905 Acta*, 72(7), 1824–1836.  
906



- 907 Sturt, H. F., Summons, R. E., Smith, K., Elvert, M., & Hinrichs, K. U. (2004). Intact polar  
908 membrane lipids in prokaryotes and sediments deciphered by high-performance  
909 liquid chromatography/electrospray ionization multistage mass spectrometry—new  
910 biomarkers for biogeochemistry and microbial ecology. *Rapid communications in*  
911 *mass spectrometry*, 18, 617–628.  
912
- 913 Teske, A., Callaghan, A. V., & LaRowe, D. E. (2014). Biosphere frontiers of subsurface  
914 life in the sedimented hydrothermal system of Guaymas Basin. *Frontiers in*  
915 *Microbiology*, 5, 362.  
916
- 917 Teske, A., De Beer, D., McKay, L. J., Tivey, M. K., Biddle, J. F., Hoer, D., Lloyd, K.G.,  
918 Lever, M.A., Røy, H., Albert, D.B & MacGregor, B. J. (2016). The Guaymas Basin  
919 hiking guide to hydrothermal mounds, chimneys, and microbial mats: Complex  
920 seafloor expressions of subsurface hydrothermal circulation. *Frontiers in*  
921 *Microbiology*, 7, 75.  
922
- 923 Tierney, J.E., (2014). Biomarker-based inferences of past climate: the TEX<sub>86</sub>  
924 paleotemperature proxy. In H.D. Holland & K.K. Turekian (Eds.) *Treatise on*  
925 *Geochemistry* (2<sup>nd</sup> Ed.) 12, 379-939.  
926
- 927 Uda, I., Sugai, A., Itoh, Y. H., & Itoh, T. (2001). Variation in molecular species of polar  
928 lipids from *Thermoplasma acidophilum* depends on growth temperature. *Lipids*, 36,  
929 103–105.  
930
- 931 Wakeham, S. G., Lewis, C. M., Hopmans, E. C., Schouten, S., & Sinninghe Damsté, J. S.  
932 (2003). Archaea mediate anaerobic oxidation of methane in deep euxinic waters of  
933 the Black Sea. *Geochimica et Cosmochimica Acta*, 67, 1359–1374.  
934
- 935 Weijers, J. W., Schefuß, E., Kim, J. H., Sinninghe Damsté, J. S., & Schouten, S. (2014).  
936 Constraints on the sources of branched tetraether membrane lipids in distal marine  
937 sediments. *Organic Geochemistry*, 72, 14-22.  
938
- 939 Weijers, J. W., Schouten, S., van den Donker, J. C., Hopmans, E. C., & Sinninghe  
940 Damsté, J. S. (2007). Environmental controls on bacterial tetraether membrane lipid  
941 distribution in soils. *Geochimica et Cosmochimica Acta*, 71, 703–713.  
942
- 943 Wuchter, C., Schouten, S., Wakeham, S. G., & Sinninghe Damsté, J. S. (2005). Temporal  
944 and spatial variation in tetraether membrane lipids of marine Crenarchaeota in  
945 particulate organic matter: Implications for TEX<sub>86</sub>  
946 paleothermometry. *Paleoceanography*, 20, doi 10.1029/2004PA001110.  
947
- 948 Yoshinaga, M. Y., Kellermann, M. Y., Rossel, P. E., Schubotz, F., Lipp, J. S., &  
949 Hinrichs, K. U. (2011). Systematic fragmentation patterns of archaeal intact polar  
950 lipids by high-performance liquid chromatography/electrospray ionization ion-trap  
951 mass spectrometry. *Rapid Communications in Mass Spectrometry*, 25, 3563–3574.  
952



- 953 Zeng, Z., Liu, X. L., Farley, K. R., Wei, J. H., Metcalf, W. W., Summons, R. E., &  
954 Zhang, Y. G., Pagani, M., & Wang, Z. (2016). Ring Index: A new strategy to  
955 evaluate the integrity of TEX<sub>86</sub> paleothermometry. *Paleoceanography*, 31, 220–232.  
956
- 957 Zhang, Y. G., Zhang, C. L., Liu, X. L., Li, L., Hinrichs, K. U., & Noakes, J. E. (2011).  
958 Methane Index: A tetraether archaeal lipid biomarker indicator for detecting the  
959 instability of marine gas hydrates. *Earth and Planetary Science Letters*, 307, 525–  
960 534.  
961
- 962 Zhu, C., Lipp, J. S., Wörmer, L., Becker, K. W., Schröder, J., & Hinrichs, K. U. (2013).  
963 Comprehensive glycerol ether lipid fingerprints through a novel reversed phase  
964 liquid chromatography–mass spectrometry protocol. *Organic Geochemistry*, 65, 53–  
965 62.